

Automatic Detection of Choroidal Hyperpermeability using Machine Learning Strategies

João Geraldes Salgueiro

Thesis to obtain the Master of Science Degree in

Computer Science and Engineering

Supervisors: Prof. Daniel Simões Lopes
Doctor Diogo Gonçalo Reis Cabral

Examination Committee

Chairperson: Prof. João Pedro Faria Mendonça Barreto
Supervisor: Prof. Daniel Simões Lopes
Member of the Committee: Prof. Jacinto Carlos Marques Peixoto do Nascimento

November 2023

Declaration

I declare that this document is an original work of my own authorship and that it fulfills all the requirements of the Code of Conduct and Good Practices of the Universidade de Lisboa.

Acknowledgements

Firstly, I would like to thank my co-supervisors Dr. Diogo Cabral and Prof. Daniel Lopes for all the help, time and support they offered throughout the whole development of this work. A huge thank you to Dr. Diogo Cabral for all the time spent helping me to understand the problem at hand and also for all the dedication and effort dedicated to guiding me through the elaboration of this work.

Would also like to thank all the staff from NOA that contributed to this work with a special thank you to Dr. Pedro Cabral that provided major contributions by annotating the datasets used for this project. This work would simply not have been possible without his time-consuming effort.

I also want to thank the Vitreous Retina and Macula Consultants of New York for providing their dataset to this project. Also, a huge thank you to all the patients that agreed to provide their medical data for research purposes.

Lastly, I would like to show my gratitude to my family, friends and girlfriend that supported me and gave me motivation to persevere through hardship during all these months. Their support was the key to keep going and face all the predicaments and setbacks with a positive attitude.

Abstract

Machine Learning techniques based on deep neural semantic models have been successfully used in multiple biomedical imaging challenges. In this study, we present a new approach for the Automatic Detection of Choroidal Hyperpermeability points, on patients with Central Serous Chorioretinopathy, using Optical Coherence Tomography. This work focuses on developing an automatic pipeline that leverages machine learning techniques to generate two essential artifacts: a thickness map and a binary classification indicating the presence of choroidal hyperpermeability points. Using the connection between abnormal choroidal thickness and patterns and the presence of choroidal hyperpermeability points, our methodology uses the generated choroidal thickness maps to provide an automatic detection of choroidal hyperpermeability points. The practical application of this project is demonstrated in the context of central serous chorioretinopathy (CSCR), a condition where the automatic detection of choroidal hyperpermeability holds clinical significance. The proposed automatic pipeline has the potential to enhance diagnostic processes for CSCR, providing a more efficient and reliable method for identifying choroidal hyperpermeability points in OCT scans. Using this methodology, we achieved results of 94.46% Dice score in choroidal segmentation challenge and a classification accuracy of 81,25% of the presence of choroidal hyperpermeability points.

Keywords: Machine Learning, Ophthalmology, OCT, Choroid, Semantic Segmentation, CSCR

Resumo

Técnicas de Aprendizagem Automática baseadas em modelos semânticos neurais profundos têm sido utilizadas com sucesso em vários desafios de imagem biomédica. Neste estudo, apresentamos uma abordagem inovadora para a Detecção Automática de Pontos de Hiperpermeabilidade Coroidal em pacientes com Coriorretinopatia Serosa Central, utilizando Tomografia de Coerência Ótica (TCO). Este trabalho concentra-se no desenvolvimento de um pipeline automático que utiliza técnicas de aprendizagem automática para gerar dois artefactos essenciais: um mapa de espessuras coroidais e uma classificação binária indicando a presença de pontos de hiperpermeabilidade coroidal. Com base na relação entre a espessura e padrões anormais coroidais e a presença de pontos de hiperpermeabilidade coroidal, a nossa metodologia utiliza os mapas de espessura coroidal gerados para efetuar uma detecção automática desses pontos. A aplicação prática deste projeto é demonstrada no contexto da coriorretinopatia serosa central (CSCR), uma condição em que a detecção automática de hiperpermeabilidade coroidal é clinicamente significativa. O pipeline automático proposto tem o potencial de aprimorar os processos diagnósticos para CSCR, fornecendo um método mais eficiente e confiável para identificar pontos de hiperpermeabilidade coroidal em exames de TCO. Utilizando esta metodologia, alcançamos resultados de 94,46% de índice Dice na segmentação coroidal e uma precisão de classificação de 81,25% na presença de pontos de hiperpermeabilidade coroidal.

Palavras Chave: Inteligencia Artificial, Oftamologia, TCO, Coroide, Segmentação de Imagem

Table of Contents

Declaration.....	i
Acknowledgements.....	iii
Abstract	v
Resumo	vii
Table of Contents	ix
List of Figures	xi
List of Tables.....	xv
List of Abbreviations	xvii
1. Introduction	1
1.1 Human eye, the choroid, and its impact on retinal health	2
1.2 Central Serous Chorioretinopathy.....	4
1.2.1 Main Characteristics and therapeutics	4
1.2.2 Choroidal Hyperpermeability and other Abnormalities as a biomarker of CSCR	6
1.3 Indocyanine Green Angiography.....	9
1.3.1 Scanning Protocol.....	9
1.3.2 Analysis on the advantages and disadvantages of ICGA in the context of CSCR	10
1.4 Optical Coherence Tomography (OCT).....	12
1.4.1 Scanning Protocol.....	12
1.4.2 OCT scans have a replacement of ICGA scans.....	14
1.5 Deep Neural Semantic Segmentation	17
1.5.1 Convolutional Neural Networks in the context of Image Segmentation	17
1.5.2 U-Net and U-Net++	18
1.5.3 Dilated Residual U-Net	20
1.5.4 SegResNet	21

1.6 Automatic Image Classification	22
2. Related Work.....	23
2.1 Convolutional Neural Networks in Choroidal Segmentation	23
2.2 Patch-based vs Semantic segmentation in Choroidal Segmentation.....	24
2.3 UWF OCT in feature analysis of choroids vasculature	26
2.3 Overview of relevant literature	27
3. Implementation	29
3.1 General Architecture Overview.....	29
3.2 Choroidal Segmentation & Thickness Map Generation	30
3.3 Thickness Map Classification.....	33
4. Results	35
4.1 Evaluation Metrics.....	35
4.2 Choroidal Segmentation Results	37
4.3 Thickness map classification Results.....	41
4.4 Other Contributions	42
5. Discussion.....	43
5.1 Choroidal Segmentation Challenge results analysis	43
5.2 Thickness Map Generation and Classification result analysis.....	44
5.3 Points of Improvement	47
6. Conclusion	49
References.....	51

List of Figures

- Figure 1: Anatomy of the Human Eye.** The human eye is anatomically divided into two main zones: Posterior and anterior. The posterior zone is comprised of important structures for the processing of visual information such as the retina, the macula, and the optic nerve. Conversely, the anterior zone is composed of other structures like the iris, the cornea, or the pupil³. 2
- Figure 2: Schematic Illustration of the transport processes supported by the choroid's choriocapillaris.** Transactions between the choroid and retina of oxygen, nutrients and metabolic wastes performed through fenestrated choriocapillaris. Adapted from Moussa A. Zouache *et al.* (2018)¹². 3
- Figure 3: Horizontal sectional image of serous detachment of the retina.** The example, taken using Swept-Source Optical coherence tomography, shows in the middle between the choroid and retina an accumulation of liquid and central serous detachment. Adapted from Ota et al. 2013)²¹. 5
- Figure 4: Schematic illustration of Laser Photocoagulation treatment for CSCR.** The image depicts a focused laser beam being applied to the affected area of the retina. The laser burns created by the procedure help seal off leaking blood vessels and promote reabsorption of accumulated fluid, aiming to stabilize retinal detachment caused by fluid accumulation²⁹. 6
- Figure 5: Indocyanine Green Angiography (ICGA) scan of an example of enlarged vortex veins.** The arrow points to the area where the enlargement of these vessels is more severe. There are a multitude of underlying conditions that can cause this, including some ocular disorders, inflammation, or even other conditions like diabetes. Adapted from Abendroth et al. (2017)³⁵. 7
- Figure 6: ICGA scan of a patient with imbalanced choroidal venous drainage.** By dividing the image into four quadrants centered on the optic nerve it is clearly visible that there is an imbalance in venous drainage. The scan belongs to a 75 year old patient with CSCR³⁸. 8
- Figure 7: Schematic Illustration of the diffusion of Indocyanine Green in the choroid.** The injected ICG (marked as the green dots) remains intravascular until it reaches the choroid but then spreads into the choroidal stroma, the connective tissue layer within the choroid, supporting blood vessels and other structures, a specific layer of the choroid composed mostly by vascular tissue, through the fenestrated choriocapillaris. Adapted from Herbort et al. (2021)⁴¹. 9
- Figure 8: Ultrawide field (UWF) ICGA scan with zoom on pachyvessels:** This figure demonstrates the ability of ICGA scans of providing clear in vivo images of choroidal vasculature and in this particular case

of pachyvessels, which is a term to describe dilated choroidal vessels that do not narrow towards the posterior pole ⁴³	10
Figure 9: ICGA scan of patient diagnosed with CSCR and annotated with the point of choroidal hyperpermeability. In the scan the area marked inside the orange box details a section of choroidal leakage associated with choroidal hyperpermeability. The zone is clearly distinguishable from the surrounding area due to it being more fluorescent. This happens because on the side there is a concentration of ICG dye. The scan was facilitated for the project by the Vitreous Retain Macula Consultants of New York (VRMCNY).	11
Figure 10: Illustration of how Optical Coherence Tomography Machines use light beams to scan tissue. The light beam emitted by the machine gets split into two paths one towards the tissue and another towards a mirror. The reflected beams then get fused and analyzed by photon detector. Adapted from Whaston Photonics ⁴⁵	12
Figure 11: Illustration of the the orientation of the volume scan outputed by OCT machine. The Volume scan when “sliced” alongside the x-axis or the y-axis results in a two-dimensional image, comonly reffered to as B-scan. The enface plan refers to any image that is perpendicular to the z-axis ²	13
Figure 12: Example of OCT B-scan with the layer anotated to it. On the B-scan the multiple layers that compose the posterior zone of the eye are clearly visible. On the upper part the retina, then separating the retina from the choroid we have the BM and then on the deeper parts we have the choroid and then the sclera.	14
Figure 13: Illustration of the process necessary to transform an OCT volume scan into a choroidal enface scan and thickness map. Firstly, the Cubic scan is “sliced” into multiple B-scans which are then annotated with the upper and lower limit of the choroid. The values are then composed into two-dimensional arrays which are translated into gradients.	16
Figure 14: Graphical representation of a U-Net architecture. On the left side we can observe the layers that compose the encoder and on the right the decoder’s composition. The skip connection is also represented by the grey arrows in the middle ⁵⁹	19
Figure 15: Graphical representation of a U-Net++ architecture. The network begins with an encoder sub-network (backbone) followed by a decoder sub-network. There are skip pathways (marked in green and blue) that connect the two sub-networks ⁶²	20
Figure 16: Graphical Representation of the original SegResNet architecture. The architecture takes advantage of the use of repeated ResNet blocks coupled with normalization blocks ⁶⁶	21

Figure 17: Section of OCT B-scan with two of the CSJ annotated. The border in the red square has a loss less pixel contrast then the green square. This happens because of the irregular light refraction on the upper layers, causing the task of choroidal segmentation to be harder on the CSJ than on the BM which is much better defined.	23
Figure 18: Graphical Illustration of how patch-based segmentation works. The input image is partitioned into small patches with then are assigned a labeled. Then the patches are overlapped into one output image ⁶⁸	25
Figure 19: Schematic representation of the proposed architecture. The overall pipeline is divided into two components, a choroidal segmentation model and a choroidal hyperpermeability (CH) classification model. The first component intakes the three-dimensional OCT scan and through a multitude of transformations outputs an enface scan and a thickness map. The second section is trained for detecting CH using thickness maps with an ICGA scan taken to confirm the presence of ICGA and thus serving as ground truth label for training.	30
Figure 20: OCT B-scans from the validation set used anottated by the trained SegResNet (left) and anottated by field professionals (right). Figure 20.1 A and B are B-scans taken from a patient with CSCR and extreme thickning of the choroid, Figures 20.2 A and B are from an healthy subject and 20.3 A and B were taken from patient with CSCR but from the section that contains the optic nerve.	38
Figure 21: Thickness maps generated from patients with CSCR (right – 21.2, 21.4) and from healthy patients (left 21.1, 21.3). In most cases, patients with CSCR display a more uneven choroidal layout with areas of extreme thickness present. As shown by 21.1 and 21.3 (both taken from healthy patients) healthy choroidal thickness maps have much more distributed layout without any submit changes in thickness.	39
Figure 22: Thickness maps generated from patients with CSCR that have choroidal hyperpermiability points (top) and ICGA scans from the same patients with the areas anottated by professionals. The scans were aligned using the superficial vessels using the enface scan and ICGA. On these presented scans the areas of choroidal hyperpermiability cohincide with areas of extreme thickning.	40
Figure 23: Composition of three thickness maps generated from 15mm-by-9mm OCT scans. This was achieved by adapting the proposed pipeline to accommodate the new sizes. Scan in the left is before the treatment and the right after treatment. The blue areas of choroidal thickening in the top half of the scan (granulomas) disappear after the therapeutics.	42
Figure 24: Composition of two automatically segmented OCT B-scans by the proposed pipeline. Figure 24-A is an OCT B-scan taken from a patient with CSCR thus having lower contrast in the CSJ in the area	

highlighted where the model struggles. Figure 24-B demonstrates that the model segments around the optic nerve area with high accuracy,	44
Figure 25: Two thickness maps generated from an elderly patient with CSCR. Figure 26-A is the left eye and Figure 26-B the right eye. In both cases the image is very choppy and lacks a clear and natural progression of choroidal thickness which is expected. The image has banding noise. The lack of quality can be seen by the lack of a defined optic nerve contour. This can happen when the scan has too much noise due to the patient not being able to stay still while the scan takes place.	45
Figure 26: Two thickness maps generated by the proposed pipeline, both with points of choroidal hyperpermeability. Figure 27-A presents a central area with abnormal thickening and pattern, but Figure 27-B does not display any abnormal choroidal distribution although ICGA scan confirms the presence of choroidal hyperpermeability. These outlier cases where the thickness maps are “normal” are where the trained models struggle to identify if there are points of choroidal hyperpermeability.	46
Figure 27: Two Swept Source OCT B-scans, Figure 28-A untreated and Figure 28-B with the denoising algorithm applied to it. The algorithm works especially well on increasing the average pixel contrast on the CSJ making simple segmentation techniques 17% more accurate.....	48

List of Tables

Table 1: Overview of Relevant Literature. In this table it is presented the studies that address choroidal segmentation, which models and data were used and the results obtained.....	27
Table 2: Deep semantic segmentation chosen for the choroidal segmentation task. All the models chosen are UNET variation: UNET, UNET++, DRUNET and SegResNet.....	31
Table 3: Dataset used for choroidal segmentation model training dataset (CSCR NV: Central Serous Chorioretinopathy Neovascularized, CSCR C: Central Serous Chorioretinopathy Cronic, PN: Pachychoroid Neovascularized, PNN: Pachychoroid not vascularized	31
Table 4: Choroidal Segmentation results using the previously mentioned metrics and eval set (Dice coefficient, Accuracy, Recall and Precision)	37
Table 5: Results obtained by the trained Automatic Choroidal Hyperpermeability Detection Model. To evaluate the model the metrics used were Accuracy, Recall and Precision.	41

List of Abbreviations

BM	Bruch's Membrane
CNN	Convolutional Neural Network
CNV	Choroidal Neovascularization
CH	Choroidal Hyperpermeability
CSCR	Central Serous Chorioretinopathy
CSJ	Choroidal Scleral Junction
DRUNET	Dilated Residual U-Net
FA	Fluorescein Angiography
GER	Grupo de Estudos da Retina
ICG	Indocyanine Green
ICGA	Indocyanine Green Angiography
IOP	Intraocular Pressure
IVA	Intervortex Anastomoses
MSE	Mean Square Error
NN	Neural Network
NOA	Nucleo Oftamologico de Almada
ONH	Optic Nerve Head
ReLU	Rectified Linear Unit
SPO	Sociedade Portuguesa de Oftalmologia
Tahn	Hyperbolic Tangent
TVST	Translational Vision Science & Technology
VRMCNY	Vitreous Retina and Macula Consultants of New York

1. Introduction

Central Serous Chorioretinopathy (CSCR) is a retinal disorder characterized by the accumulation of fluid in the subretinal space, leading to vision impairment. Early and accurate diagnosis of Choroidal Hyperpermeability (CH), a key hallmark of CSCR, is critical for effective treatment and patient care. In recent years, advancements in medical imaging and machine learning techniques have opened new avenues for improving the diagnostic process¹.

Optical Coherence Tomography (OCT) is a powerful and non-invasive imaging technique that provides high-resolution, images of biological tissues, particularly in ophthalmology, where it enables detailed assessment of critical ocular structures and with a particular set of transformations can provide information about the vessel's vasculature and thickness².

The main aim of this project is to create a system that can effectively identify a condition called choroidal hyperpermeability using scans from a medical imaging technique called OCT. Choroidal hyperpermeability is a situation where blood vessels in a specific part of the eye behave abnormally, and detecting this accurately is crucial for diagnosis. In addition to spotting this condition, we also want our system to generate maps that show the thickness of different parts of the eye. These maps can be like a special kind of picture that helps doctors get more information for making diagnoses. So, it is like giving doctors an extra tool to better understand what is happening inside the eye.

This work presents a comprehensive exploration into the realm of machine learning techniques, specifically Convolutional Neural Networks (CNNs) and U-Net segmentation, applied to Optical Coherence Tomography (OCT) scans with a focus on the automatic detection and classification of CH points within choroidal thickness maps. This research aims to bridge the gap between cutting-edge technology and clinical practice, helping healthcare professionals with a robust non-invasive tool for early CSCR detection. This work was sunmitted for grants from Grupo de Estudos da Retina (GER)³ and Sociedade Portuguesa de Oftalmologia (SPO)⁴. Also, this work is currently under review for submission to Translational vision science & technology (TVST)⁵.

1.1 Human eye, the choroid, and its impact on retinal health

The human eye is a complex organ composed of a multitude of interconnected layers of tissue. Each layer has an important role in converting light into a perceptible signal to the brain. Anatomically, the eye can be divided into two areas: Posterior and Anterior (Figure 1). The Anterior zone refers to the frontal area of the eyeball and includes the cornea, the iris and lens. The Posterior zone comprises the back part of the eyeball and contains structures like the sclera, the choroid, and the retina⁶. It is in this zone where the light gets interpreted into a signal. This process occurs mainly in the retina, which is a light-sensitive tissue in the posterior zone of the eye above the choroid and Bruch's Membrane (BM). It transforms light into electric signals which are then sent to the brain by capturing photons and passing the information along neuronal connections in electrical and chemical signals which are then decoded by the brain^{6,7}.

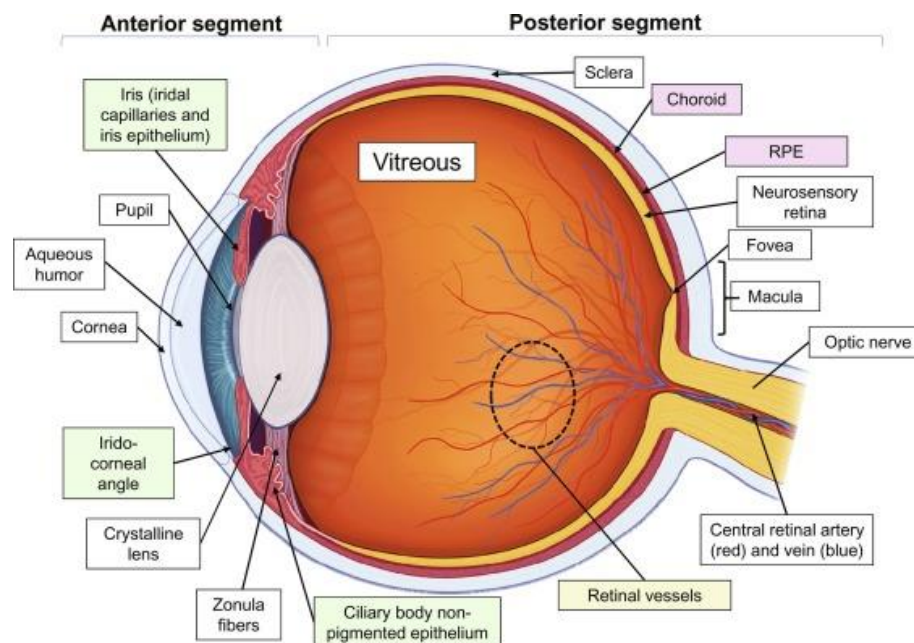


Figure 1: Anatomy of the Human Eye. The human eye is anatomically divided into two main zones: Posterior and anterior. The posterior zone is comprised of important structures for the processing of visual information such as the retina, the macula, and the optic nerve. Conversely, the anterior zone is composed of other structures like the iris, the cornea, or the pupil³.

The retina, being a highly metabolically demanding tissue, requires a constant supply of nutrients and oxygen to function properly. The choroid, a vascular layer of tissue situated between the retina and the sclera, plays a crucial role in providing the retina with these elements⁹. The choroid contains a dense network of blood vessels that serve to transport oxygen and nutrients, like glucose and vitamins, to the retina. Oxygen is crucial for a functioning retina due to the photoreceptor cells needing a constant supply of it in order to capture light signals¹⁰. Furthermore, any metabolic waste product is passed onto the choroid to be carried away from the retina and eliminated from the human body¹¹.

The choroid performs these exchanges through thin fenestrated vessels, known as choriocapillaris (Figure 2), located in the upper segment of the choroid, near Bruch's Membrane (BM), a thin layer that acts as a vascular barrier between the retina and the choroid. Moreover, by being fenestrated, the choriocapillaris are capable of diffusing oxygen and nutrients from blood vessels onto the retina and receiving its metabolic wastes.

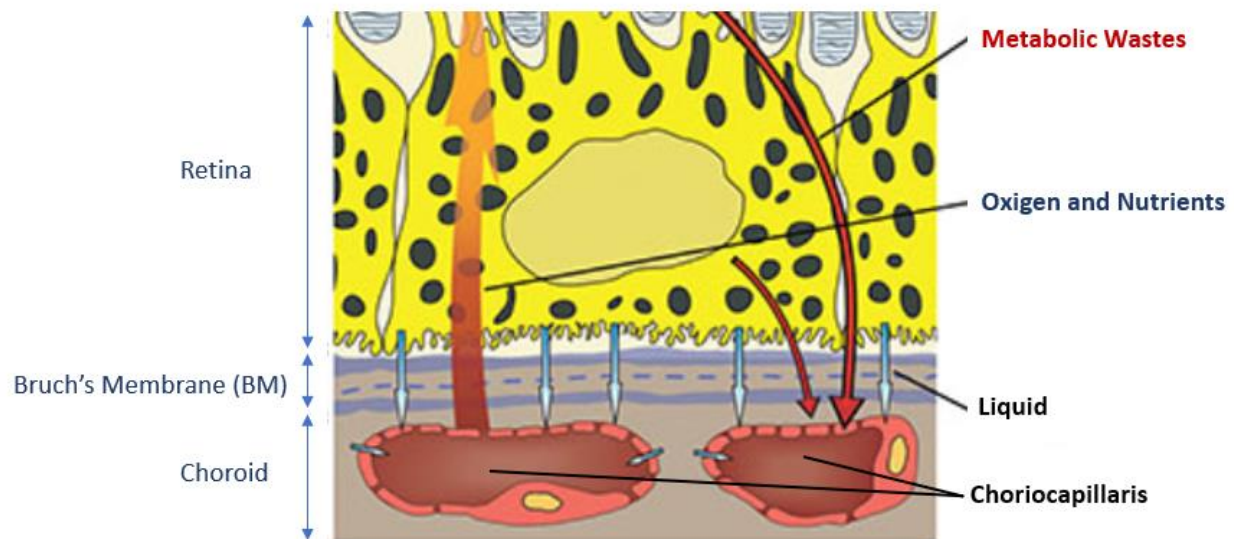


Figure 2: Schematic Illustration of the transport processes supported by the choroid's choriocapillaris. Transactions between the choroid and retina of oxygen, nutrients and metabolic wastes performed through fenestrated choriocapillaris. Adapted from Moussa A. Zouache *et al.* (2018)¹².

Furthermore, the choroid plays a key role in the balance of intraocular pressure (IOP). It does so by regulating production and drainage of aqueous humor, a clear fluid that fills the anterior portion of the eye. It also helps regulate IOP by controlling blood flow in the ciliary body, a tissue around the lens of the eye, a transparent and flexible structure located behind the iris in the anterior zone of the eye that plays a crucial role in treating the light before it reaches the retina^{9,13}.

Most of the duties performed by the choroid are not directly linked with vision but are crucial to other layers of the eye that perform such tasks, like the retina. Due to the choroid being the main source of nutrients and oxygen, any malfunction in the choroid heavily impacts retinal health. For instance, some choroidal pathologies can induce a deficient oxygen supply to the retina, promoting a well-known phenomenon as hypoxia and can induce severe damage in the retina which in turn can potentiate different deleterious human ophthalmologic pathologies^{14,15}.

1.2 Central Serous Chorioretinopathy

1.2.1 Main Characteristics and therapeutics

Central Serous Chorioretinopathy (CSCR) is a retinal disorder defined by the accumulation of subretinal fluid, mostly in the macula, an area located in the central part of the retina which is light-sensitive tissue in the surface of the retina responsible for central vision¹⁶, which can lead to vision loss^{1,17,18}. Anatomically, the retinal pigment epithelium (RPE), monolayer pigmented cells in between the retina and the underlying choroid play a key role in maintaining retinal homeostasis¹⁹. The RPE defines a barrier between the retina and the choroid and controls the transport of fluids from the choroidal vasculature and the subretinal area. Disruptions or unsettlements of RPE are directly linked to the pathogenesis of CSCR²⁰. A malfunction in this protective barrier allows for the accumulation of liquid in the subretinal space resulting in serous detachment (Figure 3) and therefore compromising the arrangement of the upper retinal layers.

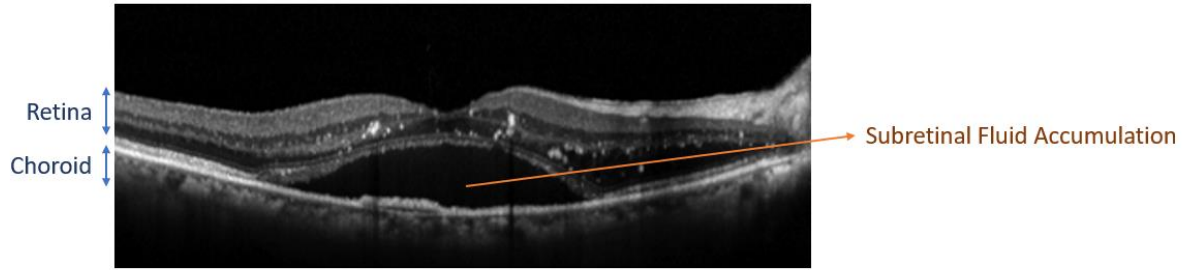


Figure 3: Horizontal sectional image of serous detachment of the retina. The example, taken using Swept-Source Optical coherence tomography, shows in the middle between the choroid and retina an accumulation of liquid and central serous detachment. Adapted from Ota *et al.* 2013)²¹.

The exact biologic mechanisms that lead to RPE dysfunction are not fully understood however there have been identified some risk factors that exponentiate its development like physiological stress or hormonal imbalances like high levels of endogenous or exogenous glucocorticoids^{17,22}, a group of steroid hormones produced by the adrenals glands that have a crucial role in regulating metabolism, immune responses, and stress responses^{23,24}. The symptoms of CSCR often involve central vision problems like reduced visual accuracy, blurred, distorted central vision and difficulty in differentiating colors²⁰. Severity and duration may vary accordingly with age and sex. Studies have found that it primarily affects working-aged males²⁵. Despite most cases of CSCR resolving spontaneously within a few months some patients have the symptoms persist. In these cases, the treatment strategies are aimed at reducing the accumulation of subretinal fluid and RPE recovery. Some lifestyle modifications like stress reducing techniques or the avoidance of corticosteroids, another class of steroid hormones naturally produced by the adrenal glands and also very commonly used as therapeutics²⁶.

In more persistent cases or with recurrent subretinal fluid accumulation there is the need for laser photocoagulation¹ (Figure 4), a procedure where a physician uses a laser to create small burns in the affected areas of the retina. The laser burns seal off leaking blood vessels in the choroid and help the body reabsorb the accumulated liquid^{27,28}. However, this procedure is not recommended for all cases (because) due to the risks associated with it. The treatment can cause some lesions to the macula and alter permanently the patient's vision hence the decision to proceed with the treatment falls under the clinician following the case who takes into consideration the location and extent of the fluid leakage in

the patient²⁸. Therefore, clinicians require some sort of *in vivo* imaging of the affected areas in order to have enough information to make a correct decision.

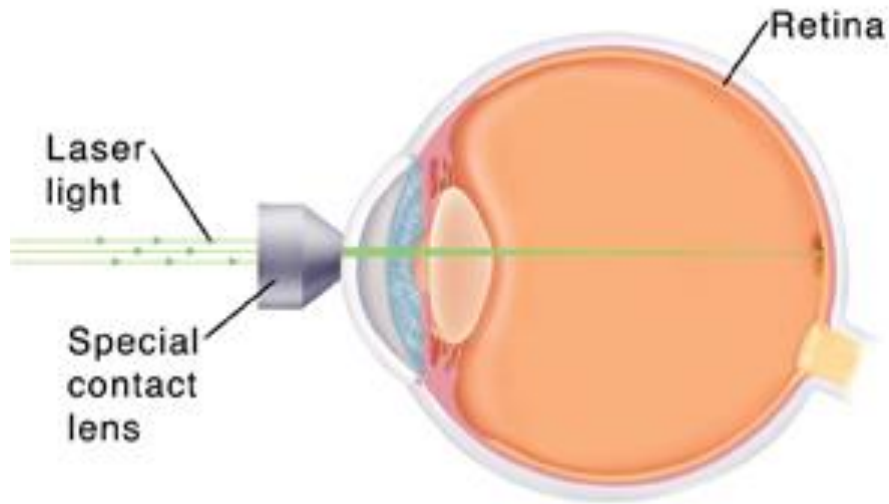


Figure 4: Schematic illustration of Laser Photocoagulation treatment for CSCR. The image depicts a focused laser beam being applied to the affected area of the retina. The laser burns created by the procedure help seal off leaking blood vessels and promote reabsorption of accumulated fluid, aiming to stabilize retinal detachment caused by fluid accumulation²⁹.

1.2.2 Choroidal Hyperpermeability and other Abnormalities as a biomarker of CSCR

For a considerable amount of time, scientists struggled to reach a consensus on what are the principal biomarkers to identify CSCR. Some studies pointed to alterations in the RPE¹, others to changes in subfoveal morphology³⁰, however, the elusive nature of the disease hindered the establishment of consensual and definitive biomarkers. Only with recent advances in biomedical imaging techniques and a deeper understanding of CSCR's pathophysiology researchers have made notable progresses in discovering new biomarkers that improved the diagnosis accuracy and helped clinicians with the choice of correct treatment for each patient.

Moreover, abnormalities in choroidal thickness and vascularity have been linked with CSCR. Some pathophysiologic mechanisms like choroidal circulatory insufficiency, the inadequate blood flow within the choroid³¹, or focal choroid hyperpermeability²⁸, the abnormal and increased permeability of choroid's blood vessels³², have been target as potential biomarkers of CSCR^{31,33}. For instance, Pang *et al.* (2014)³⁴ concluded that both the presence of dilated choroidal vessels, characterized by the enlargement or widening of blood vessels in the choroid, and the enlarged vortex vein ampullae are new potential biomarkers of CSCR (Figure 5)³⁵. Specifically, the Vortex vein ampullae is a crucial portion of the eye's drainage system as it is the main responsible for carrying blood away from the choroid and surrounding tissues. It is composed of several vortex veins, and it is situated in the choroid region. In the case of an enlargement of these veins a disruption of normal blood flow can occur thus leading to potential medical complications like an increase of IOP or even glaucoma, a group of eye conditions that can lead to optic nerve damage and vision loss or total blindness^{36,37}.

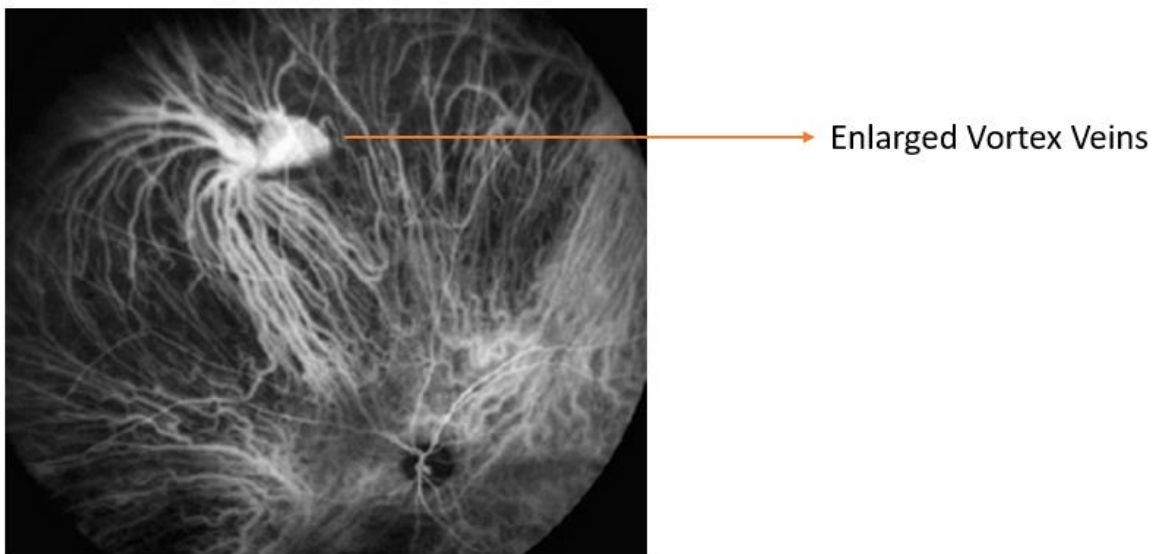


Figure 5: Indocyanine Green Angiography (ICGA) scan of an example of enlarged vortex veins. The arrow points to the area where the enlargement of these vessels is more severe. There are a multitude of underlying conditions that can cause this, including some ocular disorders, inflammation, or even other conditions like diabetes. Adapted from Abendroth *et al.* (2017)³⁵.

Moreover, recent studies revealed that imbalanced choroidal venous drainage, a phenomenon that occurs upon the disruption of outgoing venous blood flow and that can lead to an increase in IOP (Figure 6), and an imbalance in intervortex anastomoses (IVA) are characteristic biomarkers of CSCR^{31,33}. IVA refers to the presence of tiny blood channels that link neighboring vortex veins to each other. The presence of IVAs is crucial for the maintenance of correct blood flow within the choroid. Any imbalance or disruption can severely hinder venous drainage³³.

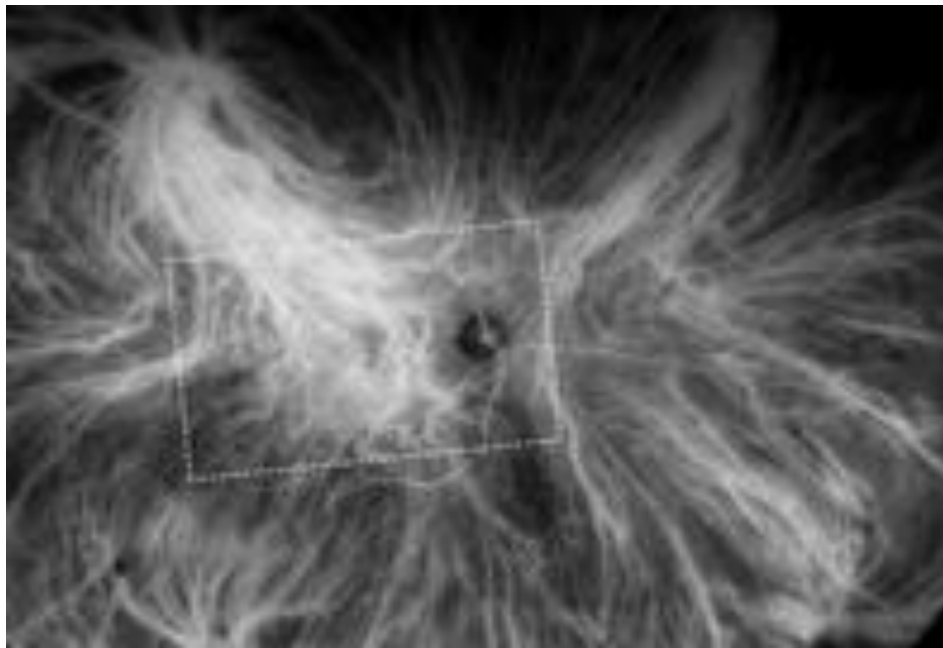


Figure 6: ICGA scan of a patient with imbalanced choroidal venous drainage. By dividing the image into four quadrants centered on the optic nerve it is clearly visible that there is an imbalance in venous drainage. The scan belongs to a 75 year old patient with CSCR³⁸.

Therefore, clinicians require *in vivo* imaging techniques in order to identify the previously mentioned biomarkers in order to provide accurate diagnosis and identify the best treatment options for CSCR. Furthermore, *in vivo* imaging techniques allow for direct visualization of internal processes and structures within a living organism, enabling clinicians to evaluate in real time any anatomical changes to the area in question.

1.3 Indocyanine Green Angiography

1.3.1 Scanning Protocol

Indocyanine Green Angiography (ICGA) has recently emerged as the gold-standard for obtaining *in vivo* imaging of the choroid. It is a very relevant imaging protocol in the context of ophthalmology that infers relevant information about anatomy, physiology and pathologies of choroidal circulation and works through the injection of a dye named Indocyanine green (ICG)³⁹.

ICG is a water-soluble tricarboyanine die that has a lot of value in multiple medical procedures especially in biomedical imaging modalities. It has been used as a contrast agent for several decades due to its outstanding fluorescent properties⁴⁰. To perform an ICGA, a small amount of ICG dye is injected intravenously into the patient's blood stream, where it quickly fuses with plasma and proteins. After a few minutes the dye reaches choroidal arteries and the choriocapillaris (Figure 7).

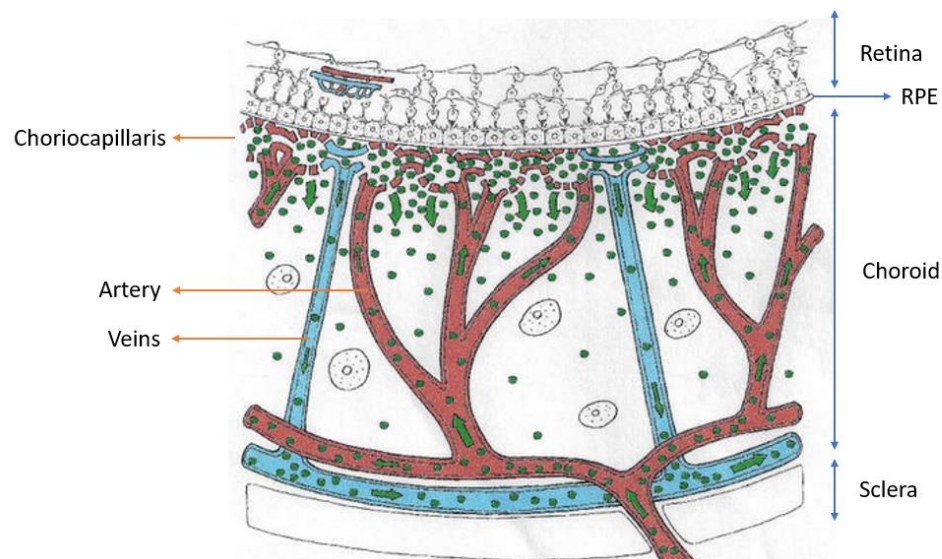


Figure 7: Schematic Illustration of the diffusion of Indocyanine Green in the choroid. The injected ICG (marked as the green dots) remains intravascular until it reaches the choroid but then spreads into the choroidal stroma, the connective tissue layer within the choroid, supporting blood vessels and other structures, a specific layer of the choroid composed mostly by vascular tissue, through the fenestrated choriocapillaris. Adapted from Herbort *et al.* (2021)⁴¹.

ICG is highly fluorescent at near infrared, thus making it perfect for imaging the deeper tissues and in particular the choroid which is located beneath the retina and BM. As the dye is circulating through the choroidal vasculature, the infrared light beams emitted from the scanning machine are absorbed by the ICG and re-emitted with a longer wavelength, therefore fluorescing. Cameras specialized in detecting that particular wavelength capture the signals create an *in vivo* image of choroidal vasculature⁴⁰. One of the major advantages of ICGA is the ability to visualize fully the choroid's vasculature (Figure 8), which in other imaging protocols like Fluorescein Angiography (FA) might not be fully suitable as that protocol in particular focuses on retinal blood vessels⁴².

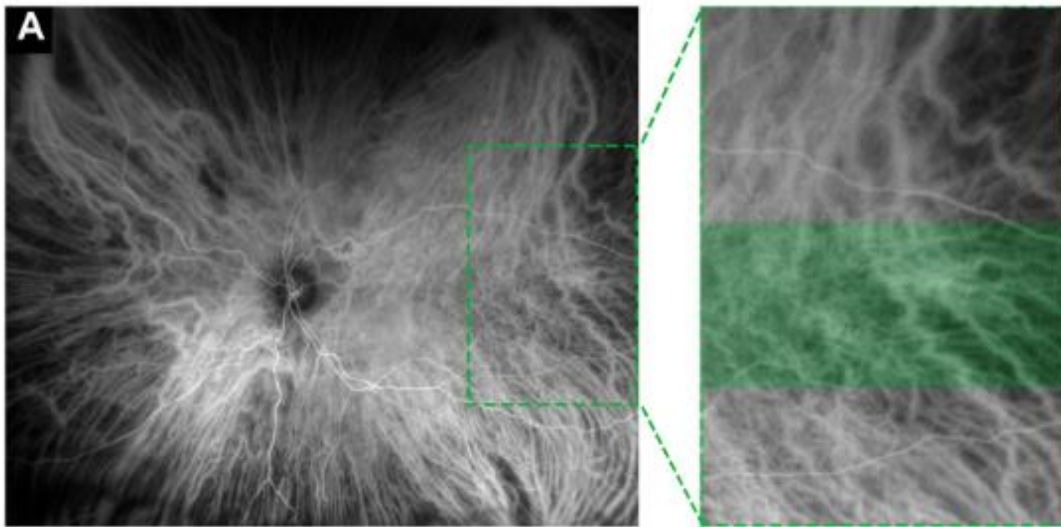


Figure 8: Ultrawide field (UWF) ICGA scan with zoom on pachyvessels: This figure demonstrates the ability of ICGA scans of providing clear *in vivo* images of choroidal vasculature and in this particular case of pachyvessels, which is a term to describe dilated choroidal vessels that do not narrow towards the posterior pole⁴³.

1.3.2 Analysis on the advantages and disadvantages of ICGA in the context of CSCR

ICGA is currently the golden standard diagnostic tool for detecting CSCR's biomarkers and the points of choroidal hyperpermeability due to providing clear enface images of choroidal vasculature. Biomarkers like imbalanced choroidal venous drainage (Figure 6) are easily identifiable through the scans.

Furthermore, the leakage points associated with choroidal hyperpermeability are detectable through ICGA thus guiding the clinician on which zone need laser treatment (Figure 9).

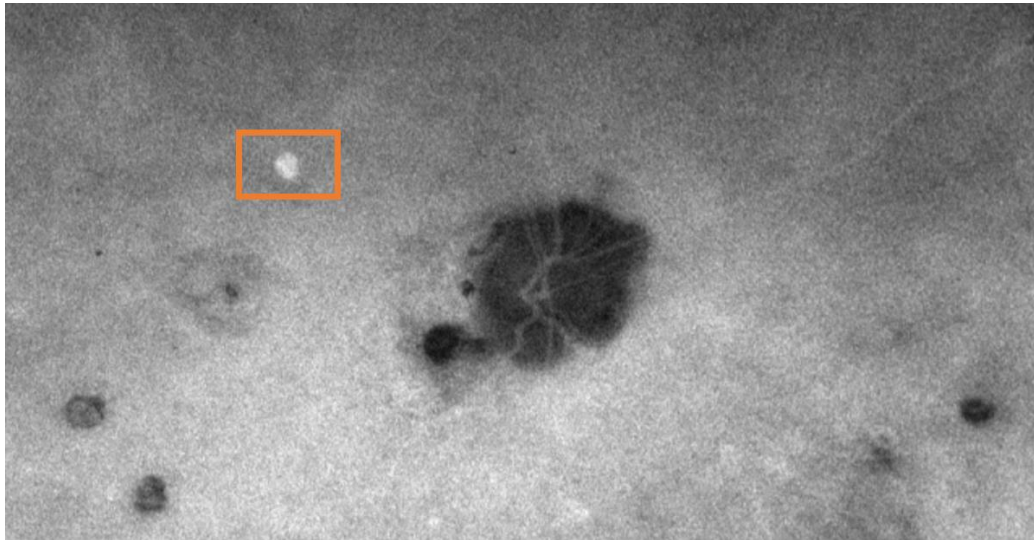


Figure 9: ICGA scan of patient diagnosed with CSCR and annotated with the point of choroidal hyperpermeability. In the scan the area marked inside the orange box details a section of choroidal leakage associated with choroidal hyperpermeability. The zone is clearly distinguishable from the surrounding area due to it being more fluorescent. This happens because on the side there is a concentration of ICG dye. The scan was facilitated for the project by the Vitreous Retain Macula Consultants of New York (VRMCNY).

Nonetheless, the imaging protocol has several drawbacks. Firstly, it is invasive due to requiring the intravenous injection of ICG dye. While ICG dye is considered safe, there is the potential risk for an allergic reaction, which can vary in severity from mild skin irritation to a severe anaphylactic response, despite this being extremely rare due to the ICG concentrations administered. Therefore, ICGA scans need to be performed in a hospital setting where there is immediate access to emergency medical equipment and personnel trained in dealing with allergic reactions. Also, ICGA scans demand previous preparation from the patient, for instance, discontinuing certain medication, drinking more water, and avoiding caffeinated drinks or tea. Lastly the scans can take up to 30 minutes to be performed^{39,40,44}. Considering the potential risks associated with ICGA and its relatively time-consuming nature, there is a growing interest in developing and implementing a more time-efficient and non-invasive imaging protocol as a preferable alternative.

1.4 Optical Coherence Tomography (OCT)

1.4.1 Scanning Protocol

Introduced in the 1990s, Optical Coherence Tomography is a non-invasive imaging technique that revolutionized the way we visualize and analyze structure of biological tissues. The fundamental principle that supports the imaging protocol is similar to ultrasound imaging, in that both techniques rely on the propagation of waves to generate detailed images of internal structures with the difference that OCT scans use light beams. The OCT machine emits a beam, low-coherence light source typically near-infrared light, that is then split into two separate paths: one is directed towards the tissue we want to scan and the other towards a reference mirror, usually referred to as the reference arm. When the light beam interacts with the biological tissue it gets partially absorbed and scattered, the remaining photons get reflected back, depending on the optical properties tissue different amounts of photons will get reflected. The reflected beams from the tissue and the machine then get combined and the pattern formed by the two beams is then inferred by a spectrometer, which is a device used to analyze the properties of light like wavelength or frequency distribution (Figure 10). Most of the commercially available OCT scan machines have an image resolution range of around 1 to 15 μm in both axial and lateral directions².

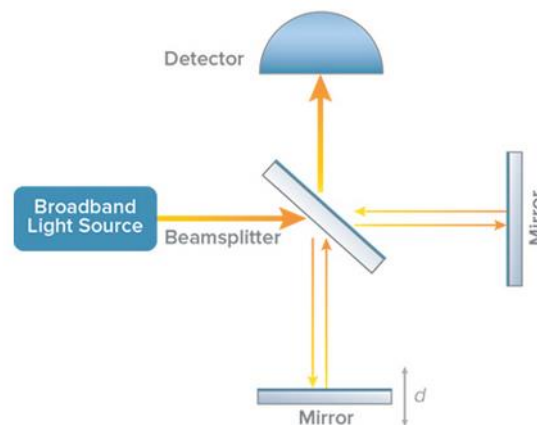


Figure 10: Illustration of how Optical Coherence Tomography Machines use light beams to scan tissue. The light beam emitted by the machine gets split into two paths one towards the tissue and another towards a mirror. The reflected beams then get fused and analyzed by photon detector. Adapted from Whaston Photonics⁴⁵.

The signals are then parsed through a complex algorithm and constructed into a cross-sectional scan of the tissue. The depth information is inferred through the time delay between the reference arm and the reflected light allowing for a three-dimensional representation of inner tissue structure⁴⁶.

In ophthalmology, it emerged as an innovative imaging technique, revolutionizing the diagnosis of a multitude of pathologies. By being non-invasive and having a high resolution, OCT is essential for clinicians to have *in vivo* imaging of ocular structures like the choroid or the retina. Due to the OCT scans being volume scans it allows clinicians to visualize cross-sections in both axis of the volume (Figure 11).

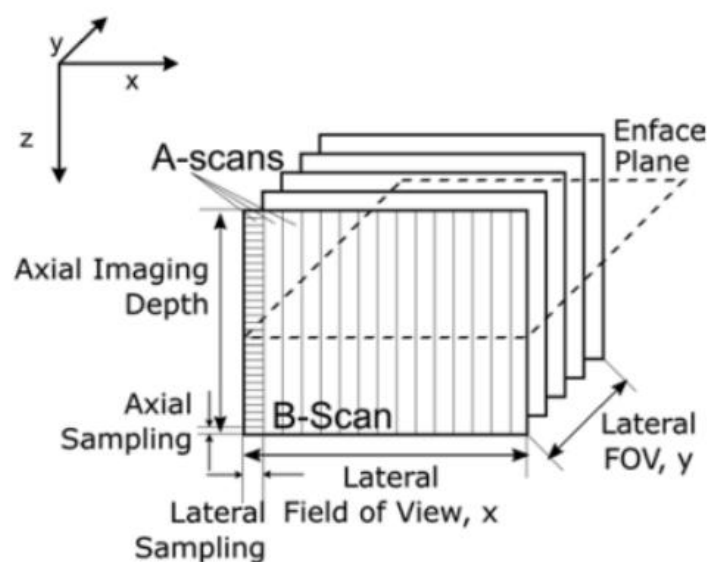


Figure 11: Illustration of the the orientation of the volume scan output by OCT machine. The Volume scan when “sliced” alongside the x-axis or the y-axis results in a two-dimensional image, comonly reffered to as B-scan. The *enface* plan refers to any image that is perpendicular to the z-axis².

When applied to the posterior zone of the eye, OCT scans allow clinicians to visualize multiple critical tissues with high detail. The retina, the optic nerve, the choroid, and the sclera are some of the major structures that can be assessed through the use of OCT scans. By slicing the volume along the x-axis or y-axis, an image containing the multiple layers of the posterior zone of the eye is generated. One scan is able to generate hundreds of B-scans, each one corresponding to one slice of the cubic volume (Figure 12).

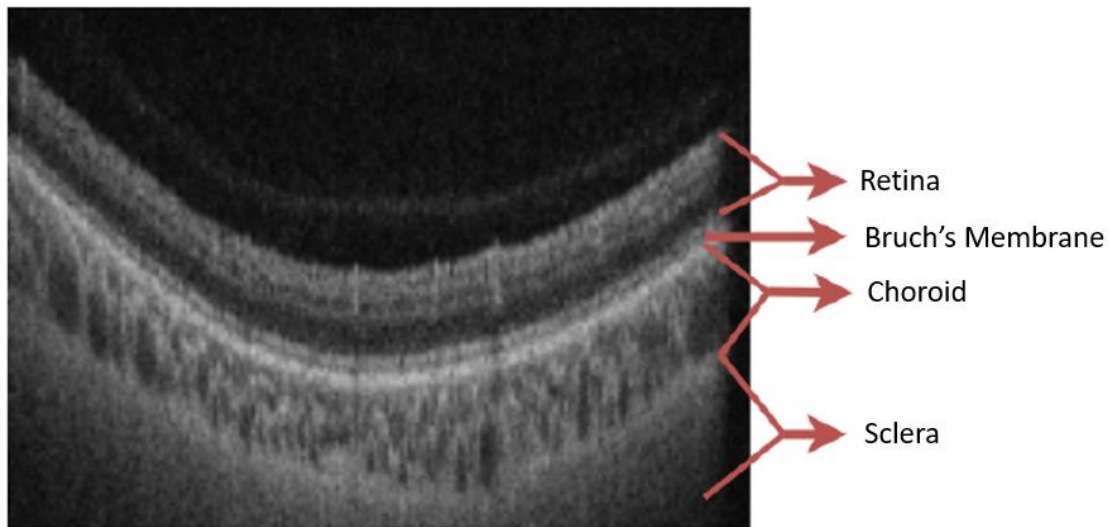


Figure 12: Example of OCT B-scan with the layer anotated to it. On the B-scan the multiple layers that compose the posterior zone of the eye are clearly visible. On the upper part the retina, then separating the retina from the choroid we have the BM and then on the deeper parts we have the choroid and then the sclera.

Nevertheless, despite providing crucial information, by itself it does not offer an offer an alternative to ICGA scans due to not providing clinicians with an *enface* projection of vasculature.

1.4.2 OCT scans have a replacement of ICGA scans

Despite the fact that OCT scans do not provide a projection of vasculature, the information provided through all the B-scans can be manipulated and constructed into an *enface* scan of a particular region of the eye. As previously mentioned, observing in detail the morphology, thickness and vascularity of the choroid is very important for clinicians in order to provide a correct diagnosis therefore an *enface* scan, such as an ICGA scan, and a choroidal thickness map provide valuable clinical information. In order to transform the cubic scan output by the OCT scanning machine into those two images, enface scan and thickness map, there are some image processing and manipulations that need to be performed. Firstly, the cube needs to “slice” into the so-called B-scans, slabs obtained by intersecting a plane perpendicular to the z-axis and moving across either the x-axis or y-axis. Depending on the modality of OCT the number of B-scans can diverge, for example a 15mm-by-15mm scan will provide us with 834 B-scans while a

12mm-by-12mm scan will only generate 500 B-scans. Then on each individual B-scan the choroid needs to be segmented, which means delimiting the upper and lower limits. The upper limit is easily identifiable by the BM which usually has a high contrast with the retina. The lower limit is the Choroidal Scleral Junction (CSJ). The most challenging part is defining the lower limit because the contrast between the sclera and the choroid is most often not the best. The pixel intensity of the choroid does not diverge a lot from the pixel intensity of the sclera due to both deeper layers of tissue and light being refracted of the top layers. Therefore, the CSJ is most often riddled with noise and plagued by low contrast especially on older patients with CSCR, where one of the symptoms is a thickened choroid.

After segmenting the choroid layer on all the individual B-scans, for the generation of the thickness map a trivial calculation of how many pixels are between the lower and upper limit alongside the z-axis is performed. For example, in a 15mm-by-15mm scan a B-scan image has a size of 834 by 834 pixels which means that we can measure thickness along the height of the image 834 times and get a one-dimensional array containing 834 values. For an *enface* scan a similar method is performed but instead of calculating a trivial distance in pixels, the average pixel intensity is calculated.

Moreover, multiple methods can be used to get an *enface* scan, like average pixel intensity, median pixel intensity or maximum pixel intensity, but the one that provided better vasculature contrast was the average pixel intensity, as it will be presented further on. Afterwards, by composing the one-dimensional arrays taken from each B-scan we can compose a two-dimensional array, that for example in a 15mm-by-15mm will be of size 834 by 834. For the *enface* scan the array is normalized and then translated into a grey scale image which details choroidal vasculature. Similarly, for the thickness map the array is translated into a color gradient, where red is a predetermined maximum value and blue the minimum value of 0, visible in the optic nerve where there is no choroid. Figure 13 illustrates the process necessary to transform an OCT scan into the previously mentioned images, the vasculature *enface* scan and the thickness map.

The biggest challenge here is that in order generate said images there is the need to segment the hundreds of B-scans. Manual segmentation, although accurate, would be too time consuming and simply not feasible. Therefore, automatic image segmentation is required.

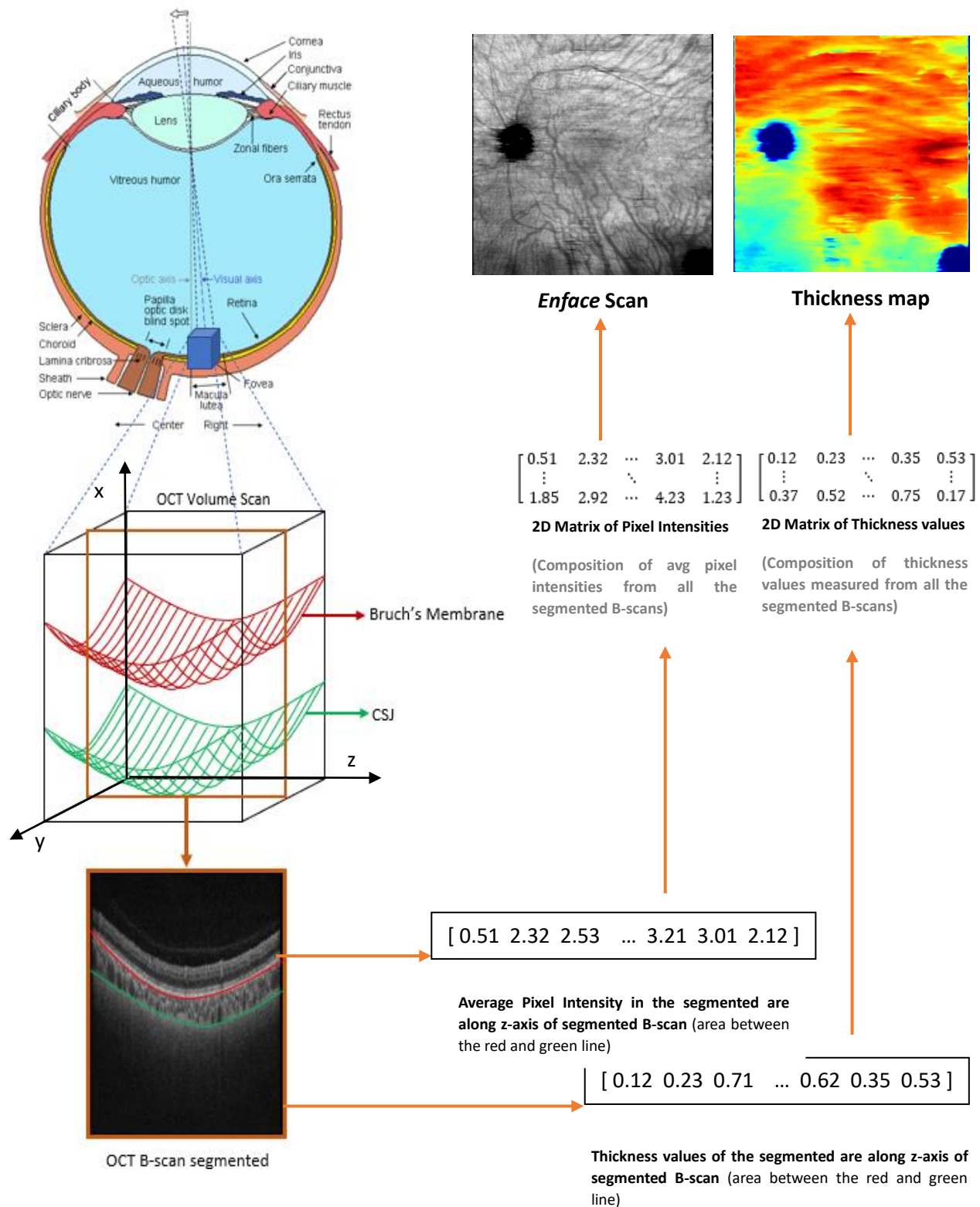


Figure 13: Illustration of the process necessary to transform an OCT volume scan into a choroidal *enface* scan and thickness map. Firstly, the Cubic scan is “sliced” into multiple B-scans which are then annotated with the upper and lower limit of the choroid. The values are then composed into two-dimensional arrays which are translated into gradients.

1.5 Deep Neural Semantic Segmentation

1.5.1 Convolutional Neural Networks in the context of Image Segmentation

In the field of Computer vision, and more specifically in the field of image segmentation, Neural Networks (NN) are a cutting-edge approach that addresses the challenging task of comprehending the visual content of images with pixel-level granularity⁴⁷. NNs are a class of Artificial Intelligence (AI) models that take heavy inspiration on how the human brain functions, more specifically on neuron behavior. The algorithm uses interconnected nodes, commonly referred to as neurons, organized into layers where each node performs a computation and propagates the value onto the next layers. Each neuron computes a weighted sum of inputs, then adds a bias term, a learnable parameter crucial for flexibility and that enables the network to capture complex relationships between outputs and inputs and applies an activation function to generate an output. An activation function is a crucial component of NN because it makes it non-linear, which means without it a NN would only be able to represent linear relationships between inputs and outputs. They allow NNs to approximate highly complex functions and capture dependencies in the data⁴⁸. The most commonly used activation functions are the Sigmoid Function, Rectified Linear Unit (ReLU) and Hyperbolic Tangent (tanh).

Training a NN involves forward propagating the input processed in order to produce predictions as output. The predictions are compared to the ground truth, which measures the prediction error. Gradient descent is an optimization algorithm employed during backpropagation. In this stage the gradients of loss function are produced for each parameter⁴⁹. The loss function is often referred to as cost function or objective function and is critical in the process of training machine learning models. Its purpose is to measure how well the model is predicting in comparison to the ground truth. The choice of loss function depends a lot on the type of problem being solved and some of the most commonly used loss functions are Mean Square Error (MSE), Binary Cross-Entropy and Hinge Loss^{50,51}. The gradients generated guide the adjustment of weights and biases, reducing the prediction error and improving the model's accuracy. Throughout the learning process the NN extracts meaningful patterns and features from the data. Furthermore, in the training process two other crucial concepts are the batch size and epochs, both of them impact the learning performance of the model. An epoch represents the full pass through the training dataset, which means in an epoch the model is fed all the training examples at

once⁵². On the other hand, batch size refers to the amount of training examples processed together in one forward pass during each epoch. Instead of updating the weights and biases after each training examples batches are used to compute gradient averages allowing for smoother actualizations of values and better learning patterns⁵³.

NNs have recently emerged as a groundbreaking method for automatic image segmentation in a multitude of fields. Convolutional Neural Networks (CNN) more specifically have become the go to architecture for this takes due to their extraordinary ability to represent intricate visual features⁵⁴. Deep CNNs are a class of NNs specially designed for processing and analyzing visual data like images. The fundamental part of CNNs are the convolutional layers which perform multiplication between small kernels and the input image, outputting feature maps that represent aspect and patterns of the inputs content⁵⁵. These feature maps then get parsed through pooling operations like max-pooling in order to down-sample and retain the most critical and informative features. These features are then subsequently passed onto the next convolutional layers creating a hierarchical feature representation of the image. CNNs are especially useful for image related tasks for their ability to absorb and isolate both global and local features^{54,55}. In the context of Semantic Segmentation, the process of portioning an image into meaningful and semantically coherent regions where each pixel is assigned a specific category or label⁵⁶, variations of Deep CNNs have emerged has state-of-the-art algorithms for a multitude of fields, like biomedical imaging and more specifically ophthalmological imaging.

1.5.2 U-Net and U-Net++

In 2015, Olaf Ronneberger *et al.* proposed a revolutionary Deep CNN architecture that quickly gained widespread popularity due to its performance in various medical image segmentation tasks like breast cancer identification or brain tumor segmentation in MRI scans^{57,58}. This architecture is specially well suited for image segmentation tasks because it possesses a high ability to capture fine details in images while maintaining spatial information⁵⁹. The U-Net architecture (Figure 14) can be divided into two main parts: the encoder and the decoder. The encoder is responsible for extracting high-level features from the input. Its structure is usually similar to normal CNN, with multiple convolutional and pooling layers. The purpose of these layers is to progressively down sample the spatial dimension of the input while increasing the number of channels. The decoder's main function is to then sample the spatial dimension

of the feature maps input from the encoder. It is usually composed of up sampling layers and skip connections that allow the decoder to combine high level semantic information with finer grained information passes from the encoder^{59,60}. The combination of both parts creates a U-shaped architecture.

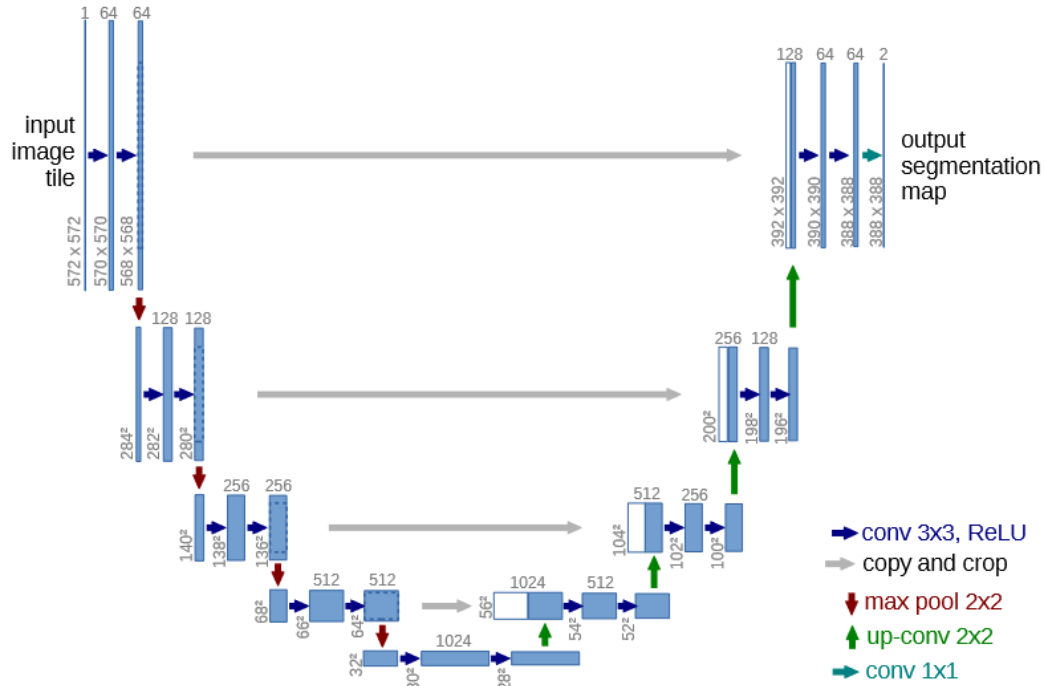


Figure 14: Graphical representation of a U-Net architecture. On the left side we can observe the layers that compose the encoder and on the right the decoder's composition. The skip connection is also represented by the grey arrows in the middle⁵⁹.

In 2018, Zhou *et al.* (2018) sought to further enhance the capabilities of the U-Net's architecture and proposed an evolutionary architecture entitled U-Net++⁶¹. The core idea was to incorporate multiple nested U-Nets, each superposed onto the previous one in order to capture progressively finer details and contextual information. There is a hierarchical organization in the network, where each layer is composed by an encoder and decoder and through the use of skip connections receive the inputs from the previous layer (Figure 15). Since its proposal, the U-Net++ has been adopted with success in a multitude of biomedical image segmentation challenges due to its ability of capturing finer-grained details than a regular U-Net architecture^{61,62}.

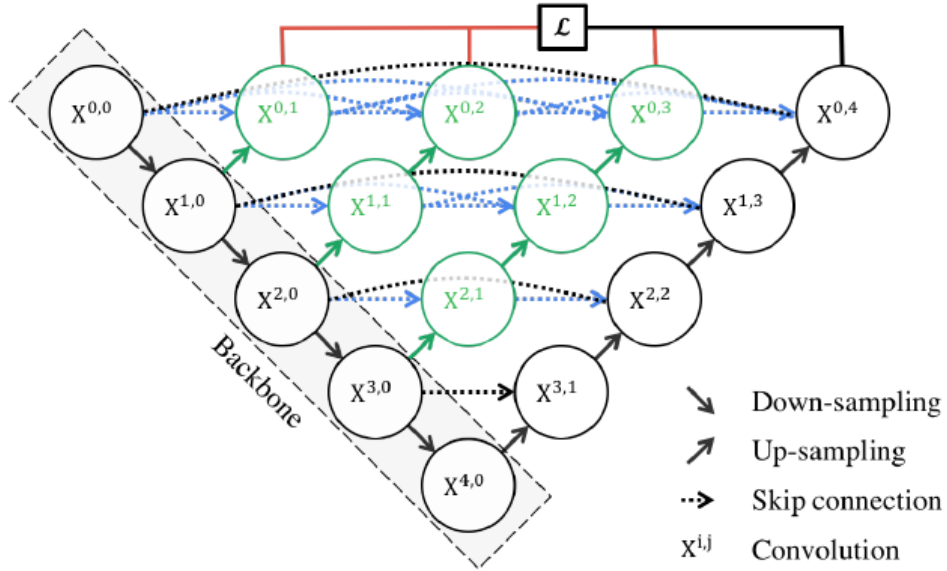


Figure 15: Graphical representation of a U-Net++ architecture. The network begins with an encoder sub-network (backbone) followed by a decoder sub-network. There are skip pathways (marked in green and blue) that connect the two sub-networks⁶².

1.5.3 Dilated Residual U-Net

In 2018, another variation of the U-Net architecture appeared. Proposed by Devalla *et al.* (2018), Dilated-Residual U-net (DRUNET) differs from a simple U-Net architecture because of its use of dilated convolutions⁶³. A dilated convolution is a variation on a convolutional that allows CNNs to have better receptive field which means a respective neuron can analyze a larger portion of the image⁶³. This is achieved by having “holes” between the elements of the convolution kernel. The dilation rate controls the size of these “holes” and larger dilation rates will also result in a larger receptive field. DRUNET also takes advantage of skip connections in order to prevent the network of becoming too deep and overfitting to the training data⁶⁴. Residual connections are a technique used in deep learning in which there are connections no adjacent to each other, allowing the network to bypass layers and connect directly to deeper or shallower layers⁶⁵. DRUNET was specifically designed to segment the optic nerve

head (ONH) in OCT scans, in this task it significantly outperformed other U-Net variations, by obtaining 0.91 Dice Coefficient (a segmentation metric used to evaluate performance) meanwhile the best result obtained by other methods was of around 0.85⁶³. This exercise showed the potential of DRUNET in the segmentation of structures from OCT scan images.

1.5.4 SegResNet

Proposed by Myronenko *et al.* (2019) SegResNet is type of CNN that is commonly used in image segmentation tasks⁶⁶. Based on the ResNet architecture, a Deep CNN that uses residual connections was designed specifically for addressing the problem of vanishing gradients. The SegResNet architecture was modified to better suit the task of image segmentation. Like the aforementioned DRUNET, it uses Dilated convolutions in order to capture long range dependencies in the input image. It also takes advantage of skip connections that prevent the model of overfitting. Furthermore, in this architecture the encoder is composed of ResNet blocks, made of two convolutions with a skip connection. Often with this architecture a variational auto-encoder, a type of generative model that learns to represent data in a latent space⁶⁷, thus regularizing the decoder's values⁶⁰.

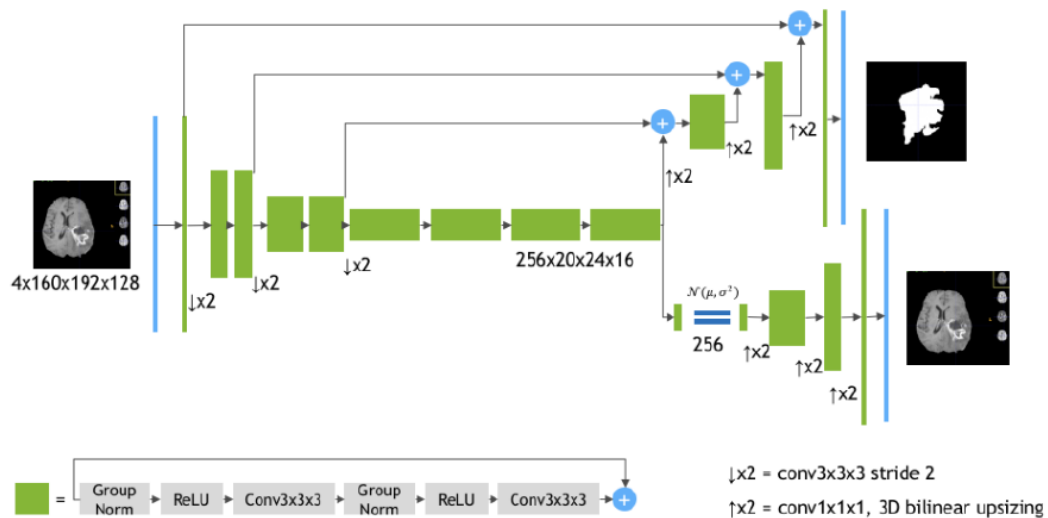


Figure 16: Graphical Representation of the original SegResNet architecture. The architecture takes advantage of the use of repeated ResNet blocks coupled with normalization blocks⁶⁶.

1.6 Automatic Image Classification

Automatic Image Classification is a very important task in the realm of computer vision, enabling machines to decipher and categorize the content of images. Furthermore, in the field of Biomedical imaging and in particular Ophthalmology imaging, automatic image classification techniques have garnered extreme relevancy in helping physicians deal with time consuming analysis of exams⁶⁸.

Among different techniques for automatic image classification, CNNs and their variations have emerged as the gold standard for most challenges due to their ability of learning intricate features directly from raw data. The use of convolutional layers enable CNNs to extract localized features and hierarchical representation, thus having the ability to discern between different categories and provide accurate classification⁶⁹.

According to the findings of Ramtohul *et al.* (2023) the points of choroidal hyperpermeability most often coincide with the areas of choroidal engorgement⁴³. This project proposes an automatic classification of the generated thickness maps accordingly with the presence of hyperpermeability points. The objective of the pipeline is to intake the OCT scan and output a Boolean flag if there is suspected presence of choroidal hyperpermeability points.

2. Related Work

2.1 Convolutional Neural Networks in Choroidal Segmentation

The project at hand introduces another formidable challenge, revolving around the intricate task of segmenting the lower bound of the choroid. The endeavor is complicated by the presence of elevated levels of light refraction, which in turn induces a degradation in the overall quality of the acquired images. From a purely image segmentation standpoint, it becomes evident that the CSJ lacks well-defined contrasts on untreated OCT B-scans, thereby intensifying the intricacy of the segmentation process. Figure 7 vividly illustrates this issue, showcasing instances where the demarcation between the sclera and the choroid exhibits irregularities and inconsistencies at various points across the image. This sporadic and unpredictable nature of contrast distribution adds a layer of complexity to the segmentation task, necessitating innovative approaches to overcome these hurdles and achieve accurate delineation of the choroid's lower boundary.

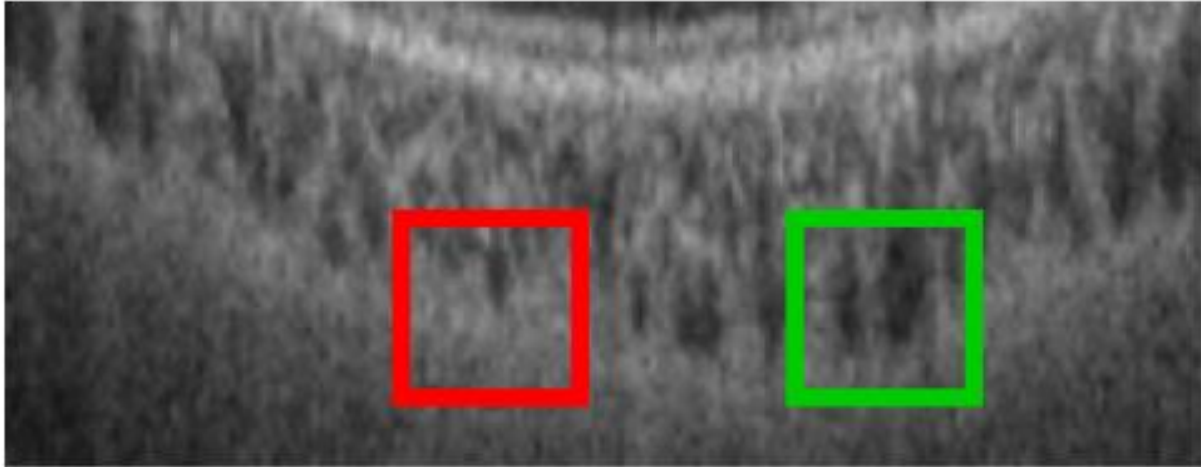


Figure 17: Section of OCT B-scan with two of the CSJ annotated. The border in the red square has a less pixel contrast than the green square. This happens because of the irregular light refraction on the upper layers, causing the task of choroidal segmentation to be harder on the CSJ than on the BM which is much better defined.

In addressing this challenge, Masood et al. (2019) devised a solution that leveraged a CNN classifier, employing both pixel-by-pixel annotation methods, whether online or offline⁷⁰. The initial step encompassed the segmentation of Bruch's membrane employing a series of structural operations applied to the image data. Subsequently, all pixels situated above the BM were rendered black, strategically minimizing the pool of classified pixels. For training the neural network, patches of size 32×32 extracted from manually segmented images were utilized. The selection of patch size emerged as a critical consideration, as it influences whether the model grapples with an overabundance of information or contends with an insufficient dataset for feature extraction⁷¹.

The chosen architecture involved the integration of a pre-trained Cifar-10 model, which was capable of accommodating the irregularities inherent in pixel classification tasks⁷². Notably, the approach also incorporated a probabilistic model to address the variability in pixel categorization. The culmination of these strategies yielded an impressive average dice coefficient of 97%, attesting to the efficacy of this methodology. Despite the commendable outcomes reported in this study, it is worth noting that the employed methodology encompassed a substantial dataset without the incorporation of specific denoising techniques.

The accuracy achieved aligned closely with results obtained from simpler architectures applied to noise-attenuated images. This observation underscores the potential for enhancing outcomes through the integration of denoising techniques and the utilization of more contemporary encoder-decoder-based neural networks. Overall, the exploration of these advanced techniques holds promise for achieving even more robust results in future endeavors.

2.2 Patch-based vs Semantic segmentation in Choroidal Segmentation

Kugelman *et al.* (2019) delve into the intricate domain of choroidal segmentation using SS-OCT scans, alongside the generation of thickness maps. This study undertakes an extensive exploration of the comparative efficacy of a multitude of techniques and models when it comes to the accuracy of this task. To facilitate this examination, the models are categorized into two distinct groups: Patch-based

methods and Semantic segmentation methods. Within the patch-based approach, the images undergo a meticulous process of segmentation by being partitioned into smaller patches.

Subsequently, each individual patch is subjected to segmentation, culminating in the assignment of pertinent labels. Following this, pixel values are computed through the meticulous analysis of overlapping patches characterized by identical labels. This process echoes the procedure depicted in Figure 8, offering a visual analogy to aid comprehension⁷³.

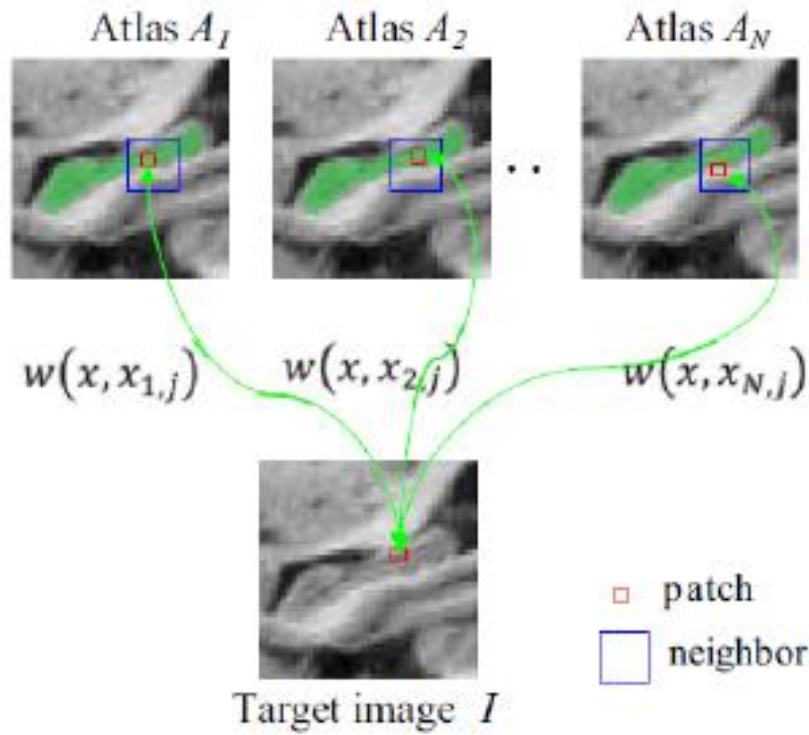


Figure 18: Graphical Illustration of how patch-based segmentation works. The input image is partitioned into small patches with then are assigned a labeled. Then the patches are overlapped into one output image⁶⁸.

The concept of semantic segmentation involves a holistic analysis of the entire image, employing sophisticated deep learning algorithms to assign categorical labels to individual pixels⁵⁶. This technique finds widespread application in image segmentation tasks necessitating the identification of specific pixel categories, exemplified by the intricate challenge posed by choroid segmentation⁵⁶.

To establish a benchmark for performance evaluation, a conventional image analysis method was employed as a baseline comparator. Notably, both patch-based methods and semantic methods exhibited superior performance in comparison to this baseline approach. Within the context of this investigation, it is deduced that patch-based methods, despite their utilization, fail to confer substantial advantages due to their lower accuracy and evaluation times.

Another point to acknowledge is that just like other studies within the same domain, this research neglects to address the potential impact of employing diverse noise attenuation techniques on performance enhancement. The forthcoming project aims to delve more profoundly into the interplay between denoising techniques and semantic segmentation strategies. By exploring the combination of these techniques, the study tries to unravel the extent to which performance can be optimized, thus contributing to a more comprehensive understanding of the nuances surrounding image segmentation in the context of choroidal analysis.

2.3 UWF OCT in feature analysis of choroids vasculature

Ramtohul *et al.* (2022) dives into an analysis aimed at discerning the potential of *enface* UWF OCT, a non-invasive technique, to identify significant features of choroidal vasculature⁴³. This study centers its focus on patients afflicted with central serous chorioretinopathy (CSC), with the primary objective of determining whether this technology can effectively detect salient attributes associated with choroidal vasculature without resorting to invasive procedures. As previously mentioned, the established benchmark for the *in-vivo* assessment of choroidal vasculature remains ICGA scans.

In this project, the choroidal structure underwent segmentation through a semi-automatic process. The amalgamation of software-driven mechanisms and manual adjustments facilitated the precise demarcation of both the lower boundary, known as the CSJ, and the upper boundary represented by the BM. By employing a series of 5 WF OCT scans, each targeted at distinct regions, a comprehensive composite *enface* UWF image spanning 31mm x 27mm was meticulously generated, as visually represented in Figure 9.

Employing analogous techniques, the study also succeeded in generating intricate choroidal thickness maps, further expanding the scope of their analysis. By comparing the ICGA scans and the generated *enface* scans it concluded that the biomarkers of CSCR are present and observable on *enface* scans and proposed the theory that the points of choroidal hyperpermeability coincide with the areas of extreme choroidal thickness.

2.3 Overview of relevant literature

In this section, we will review the most relevant studies on the subject. We will also provide a detailed look at the results and limitations of these studies, with a specific focus on how we plan to address these limitations in our project. Table 1 below summarizes each of the mentioned studies, offering a concise yet informative overview of their contexts and contributions.

Table 1: Overview of Relevant Literature. In this table it is presented the studies that address choroidal segmentation, which models and data were used and the results obtained.

Study	Segmentation Models	Data	Results
Masood <i>et al.</i> (2019)	CNN based (CSJ segmentation) + Morphologic Operations (BM segmentation)	Around 600 OCT scans	Dice Coefficient Of 97%
Kugelman <i>et al.</i> (2019)	Graph Based and Semantic Segmentation (DRUNET)	101 OCT scans from children	Dice Coefficient Of 99%
Ramtohul <i>et al.</i> (2023)	Semi-Automatic Cannon Proprietary Software	42 OCT scans	Biomarkers visibly identifiable in segmented images

Among the various segmentation techniques used, it is clear that semantic-based methods perform the best. However, many studies have overlooked the impact of denoising techniques on more advanced models. Additionally, there is a lack of in-depth exploration of choroidal segmentation in the context of WF OCT literature.

One intriguing area that has not been extensively explored in the literature is the automated classification of eye diseases using choroidal thickness maps and enface scans. This field holds great potential for further investigation. This is where our current project comes in. We aim to investigate how denoising techniques and advanced neural-based semantic segmentation methods interact in choroidal segmentation. By studying this interplay, we aim to determine if the resulting thickness maps and enface scans, produced through these improved techniques, can serve as a strong foundation for an automatic disease classification system.

3. Implementation

3.1 General Architecture Overview

Before diving deeper into the proposed methodologies, a deeper analysis of the main goals of this project is needed. From a higher level of abstraction the two goals this project hoped to achieve was study further which semantic segmentation architectures better suit the task of choroidal segmentation, taking into consideration previous studies on the matter^{43,70,73,74}, and to study the possibility of an automatic choroidal hyperpermeability detection system based on thickness maps. Therefore, there are two artifacts we sought to produce from an input OCT scan: a thickness map and a Boolean classification of the presence of choroidal hyperpermeability. Figure 19 is a graphic illustration of the proposed methodology.

The first component of the general pipeline consists of a segmentation problem. It intakes a 3-dimensional OCT scan and outputs a thickness map. The cube is firstly sliced alongside the y-axis into two dimensional images. In a 15mm by 15mm scan the cube is sliced into 834 individual scans with a width of 834 pixels. Because of the poor quality of the scan around the edges the first 75 and last 75 images are cut from the array of images, leaving us with 684 images.

The images are also trimmed to have a width of 684 pixels. The 684 individual B-scans are then segmented. As previously mentioned, segmenting all the 684 images manually would be too time consuming to be practical, therefore an automatic segmentation model is needed. As referred by study of Kugelman *et al.* (2019) semantic segmentation models are superior to other automatic segmentation techniques driven by artificial intelligence⁷⁴. This methodology is described in better detail in section 1.4.2.

The second section of the pipeline intakes the thickness map and using an automatic classification model determines if there is the presence of choroidal hyperpermeability points or not. This methodology is based on the assumption that CSCR has a particular choroidal morphology and thickness change that allows us to differentiate a healthy scan from an un-healthy one. This research is based on conclusions taken from the study of Ramtohul *et al.* (2023) that point out that there is a correlation between areas of heightened thickness and choroidal hyperpermeability points.

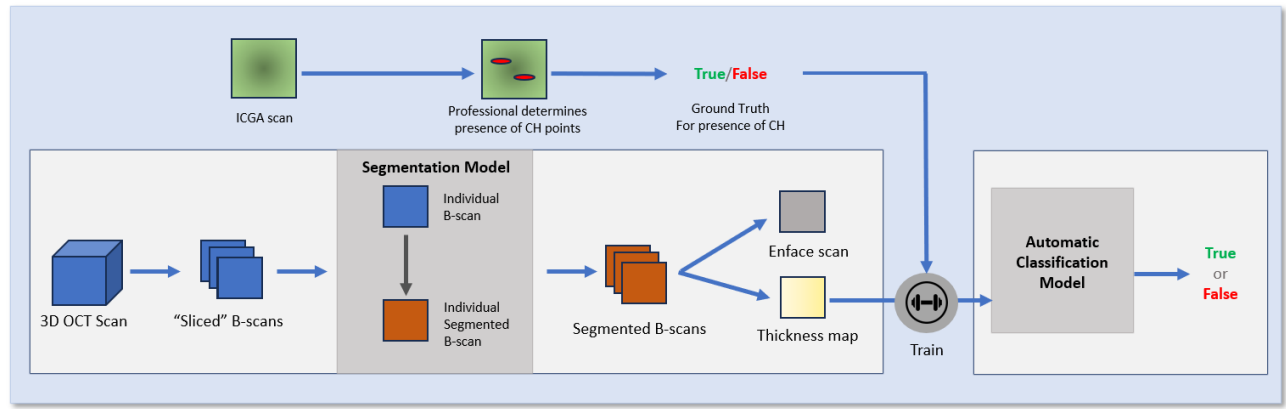


Figure 19: Schematic representation of the proposed architecture. The overall pipeline is divided into two components, a choroidal segmentation model and a choroidal hyperpermeability (CH) classification model. The first component intakes the three-dimensional OCT scan and through a multitude of transformations outputs an *enface* scan and a thickness map. The second section is trained for detecting CH using thickness maps with an ICGA scan taken to confirm the presence of ICGA and thus serving as ground truth label for training.

3.2 Choroidal Segmentation & Thickness Map Generation

As previously detailed, the first component of the pipeline will intake a cubic OCT scan. Due to the size of the cube (a 15mm-by-15mm scan has around 2 Gigabytes) with the hardware available it was not possible to work with the whole cube, thus the cube is sliced alongside the y-axis to generate 2-dimensional images, OCT B-scans. For every B-scan the choroid has to be segmented, and then along the image's y-axis calculate the thickness and average pixel intensity. By composing the values from all the OCT B-scans we can generate two artifacts: a thickness map and an *enface* scan. The thickness map is the more important of the two and it is what will be the input of the automatic classification model. The *enface* scan has the sole purpose of allowing use to juxtapose the ICGA scans with the thickness maps, aligning them through the superficial vessels which are clearly visible in both. The more complex component of this process is the automatic segmentation of the choroid. For this task this project proposes the use of deep neural semantic segmentation models, which Kugelman *et al.* (2019) determined were the superior approach in comparison to patch-based techniques⁷⁴. In this project, we chose to test 4 different variations of the UNet architecture which have shown very promising results in a multitude of biomedical imaging segmentation problems. The following table, Table 2, details the models chosen, the number of layers and size and the reason for the choice:

Table 2: Deep semantic segmentation chosen for the choroidal segmentation task. All the models chosen are UNET variation: UNET, UNET++, DRUNET and SegResNet

Model	Layers	Motivation
UNET	512x256x128	Model with widespread use across biomedical imaging challenges and also been applied to choroidal segmentation
	512x256	
UNET++	512x256x128	Evolution of the UNET architecture that achieve better performance then vanilla UNET in some problems
	512x256	
DRUNET	512x256x128	DRUNET was specifically designed for segmenting the optic nerve head (ONH) in OCT scans, where it demonstrated remarkable performance
SegResNet	512x256x128	SegResNet is a robust choice for image segmentation tasks, effectively capturing complex image structures while mitigating overfitting concerns

The dataset used for the training of the models was composed using 130 B-scan images from 30 individual scans from 16 patients with CSCR and a multitude of other pathologies as well as healthy subjects. The B-scans used were taken from a variety of sections from the scan because different sections have different choroidal morphologies. To expand the dataset, we used the following dataset augmentation techniques were used: flipping the image alongside the y-axis and adding light poison noise to simulate the noise signals from different scans. With these techniques the size of the dataset was expanded to 520 images. The following table, Table 3, contains the age and pathology distribution of the dataset collected and used in this project.

Table 3: Dataset used for choroidal segmentation model training dataset (CSCR NV: Central Serous Chorioretinopathy Neovascularized, CSCR C: Central Serous Chorioretinopathy Cronic, PN: Pachychoroid Neovascularized, PNN: Pachychoroid not vascularized)

Pathology	Male	Female
CSCR NV	2	1
CSCR C	6	2
PN	0	1
PNN	0	1
Healthy	4	3

All the models were trained using the same dataset and trained until convergence. Resizing the input images to 224x224 was a crucial decision due to hardware limitations. This helped managing memory better and made computations more efficient, given the constraints of the available hardware. Smaller images reduce memory usage and speed up processing, crucial for tasks involving convolutional neural networks. The choice of 224x224 aligns with standard practices and facilitates transfer learning with pre-trained models. In essence, this resizing strategy optimizes resources, ensuring compatibility with established models for efficient processing. The models were trained using NVIDIA GPU model GTX 1650 which has 4GB of DDR6 memory and a boosted clock speed of 1620MHz. This limited the input size and batch size we could use.

We chose to utilize Binary Cross Entropy (BCE) loss for our binary image segmentation challenge due to its simplicity and effectiveness in handling pixel-wise classification. This loss function aligns well with the nature of the task and is compatible with the U-Net derivatives we employed, ensuring stability and ease of optimization during the training process⁷⁵.

For the training the batch size was limited to 5 due to GPU memory constraints and the optimizer chosen was Adam. The choice of the Adam optimizer is justified for its efficacy in optimizing neural network parameters. Adam combines the benefits of both the Adagrad and RMSprop optimizers by dynamically adapting learning rates for each parameter based on their historical gradients.

This adaptability allows Adam to efficiently navigate complex and non-convex optimization landscapes, making it well-suited for training deep neural networks. The use of moments (first-order and second-order) helps overcome challenges like sparse gradients and accelerates convergence. Adam's popularity stems from its ability to handle a variety of tasks with minimal hyperparameter tuning, offering a robust and efficient optimization solution for training neural networks in diverse applications^{76,77}. All the models showed better learning curves using a learning rate of 0.001.

3.3 Thickness Map Classification

The second component is based on the study of Ramtohul *et al.* (2023) that states that abnormal changes in choroidal thickness and choroidal patterns are linked to CSCR and more concretely to choroidal hyperpermeability⁴³. Thus, this project proposes the development of an automatic image classification model that intakes choroidal thickness maps and outputs a Boolean classification for the presence of choroidal hyperpermeability points. Currently in order to determine if a patient has choroidal hyperpermeability points present an invasive ICGA scan is required. Through this exam physicians have empirical confirmation for such pathology. This project proposes the automatic detection of such hyperpermeability points using thickness maps generated from non-invasive OCT scans.

In this project, a binary classification system was developed to detect choroidal hyperpermeability utilizing 2D choroidal thickness maps. The foundational components of the system were built upon deep learning techniques implemented with PyTorch and the Lightning framework. The chosen model architecture was ResNet-50, a convolutional neural network pre-trained on ImageNet renowned for its efficacy in capturing intricate features within images, a critical requirement for nuanced medical image analysis⁷⁸. The preprocessing pipeline was designed to ensure uniformity in input images. Key steps included resizing images to a standardized 224x224 pixel dimension and converting them into tensors. The dataset was divided into an 80-20 split into training and validation sets to systematically evaluate the model's performance. Throughout the training phase, the Adam optimizer was employed, and the cross-entropy loss function was chosen for its appropriateness in the context of binary classification tasks. The use of PyTorch Lightning not only streamlined the training process but also provided an organized and efficient interface, incorporating essential functionalities such as logging. During the inference phase, the model parameters were loaded into a fresh instance of the model. Consistency was maintained by applying the same image transformations during inference as those used during training. The softmax function was then utilized to convert model outputs into probabilities, determining the predicted class by selecting the one with the highest probability score. In summary, this project integrates a pre-trained ResNet-50 model, PyTorch Lightning for streamlined training, and meticulous data preprocessing techniques commonly employed in the scientific field of deep learning for image classification.

The dataset used included 20 different thickness maps generated using the first component of the pipeline, and the presence of choroidal hyperpermeability points confirmed by ICGA scans. The dataset was composed using 10 positive scans and 10 negative scans. Using the same data augmentation techniques used in the first component the dataset was expanded to 80 images.

4. Results

4.1 Evaluation Metrics

As the generation of the thickness maps is a pivotal point of this project, finding the architecture that performs better at the task of choroidal segmentation in B-scans is needed. To evaluate the segmentation accuracy this project used the following metrics: Pixel Accuracy, Sorensen-Dice coefficient (Dice), Recall and Precision. Because the challenge of choroidal segmentation is a binary semantic segmentation problem this project considers a positive as pixel being classified as part of the choroid and a negative as not part of the choroid. (TP: total number of true positives, FP: total number of False positives, FN: total number of False Negatives, TN: total number of True Negatives)

Pixel accuracy is a metric that gauges the percentage of correctly classified pixels in an image. While it offers a straightforward assessment of overall performance, it has limitations. The measure can be misled by class imbalances, favoring dominant classes, and overlooking minority ones. Moreover, pixel accuracy doesn't account for the nuanced challenge of accurately delineating object boundaries, often crucial in segmentation tasks. It treats false positives and false negatives equally, neglecting the importance of precision and recall. Lastly, achieving high pixel accuracy on a specific dataset does not guarantee generalization to new data. Pixel accuracy is given by the following formula:

$$\text{Pixel Accuracy} = \frac{TP + TN}{TP + TN + FN + FP + FN}$$

The Dice coefficient is a metric commonly used in image segmentation that assesses the similarity between the predicted and true segmentation masks. It is calculated as twice the intersection of the predicted and true regions divided by the sum of their areas. The Dice coefficient addresses some of the limitations of pixel accuracy by focusing on the overlap between predicted and ground truth masks. This makes it particularly useful for tasks where precise delineation of object boundaries is crucial. Unlike pixel accuracy, the Dice coefficient is more sensitive to both false positives and false negatives, providing

a more nuanced evaluation of model performance. It ranges from 0 to 1, with 1 indicating perfect overlap. The Dice coefficient is given by the following formula:

$$Dice = \frac{2 \times TP}{(TP + FP) + (TP + FN)}$$

Recall measures the ability of a model to correctly identify all relevant pixels belonging to a specific class. It is calculated as the ratio of true positives to the sum of true positives and false negatives. Unlike pixel accuracy, recall is sensitive to false negatives, emphasizing the importance of capturing all instances of the target class. In segmentation tasks, where missing relevant pixels is critical, a higher recall indicates better model performance. However, recall alone may not provide a complete evaluation, and it is often considered alongside precision and other metrics for a more comprehensive assessment. It is assessed through the following formula:

$$Recall = \frac{TP}{TP + FN}$$

Precision gauges the accuracy of positive predictions made by a model. It is calculated as the ratio of true positives to the sum of true positives and false positives. Precision provides insights into how well the model performs when it predicts the presence of a specific class, emphasizing the importance of minimizing false positives. In segmentation tasks, high precision indicates a low rate of incorrectly labeling pixels as belonging to the target class. It is given by the following formula:

$$Precision = \frac{TP}{TP + FP}$$

By combining these metrics, we can have a good understanding of how the models are behaving and therefore make a better decision. The overall quality of the thickness maps generated is not as easily classifiable although it is directly linked to the segmentation model accuracy. The evaluation of the automatic choroidal hyperpermeability classification model is a more straight forward as a value of accuracy can provide us with a solid metric to evaluate it, although it will also be useful to look into the Precision and Recall seeing if the model tends to fail in one particular class (Negative or Positive).

4.2 Choroidal Segmentation Results

The following table (Table 4) contains the results obtained by the trained models on the evaluation set (30 OCT B-scans parsed from multiple patients with and without pathologies), with the methodologies described on section 3.2, using the metrics described on section 4.1:

Table 4: Choroidal Segmentation results using the previously mentioned metrics and eval set (Dice coefficient, Accuracy, Recall and Precision)

Model	Layers	Dice	Accuracy	Recall	Precision
UNET	512x256x128	93.81	99.04	94.12	93.77
	512x256	90.11	96.30	91.78	91.21
UNET++	512x256x128	93.98	99.05	94.12	94.07
	512x256	90.63	96.47	91.83	91.37
DRUNET	512x256x128	94.27	99.11	94.04	94.66
SegResNet	512x256x128	94.36	99.14	94.19	94.72

The following images are OCT B-scans from the set used to evaluate the models segmented with the trained SegResNet model (left) and the same OCT B-scans but annotated by experts in ophthalmology (right). The intersection between the two areas (choroid and non-choroid) is annotated in red.

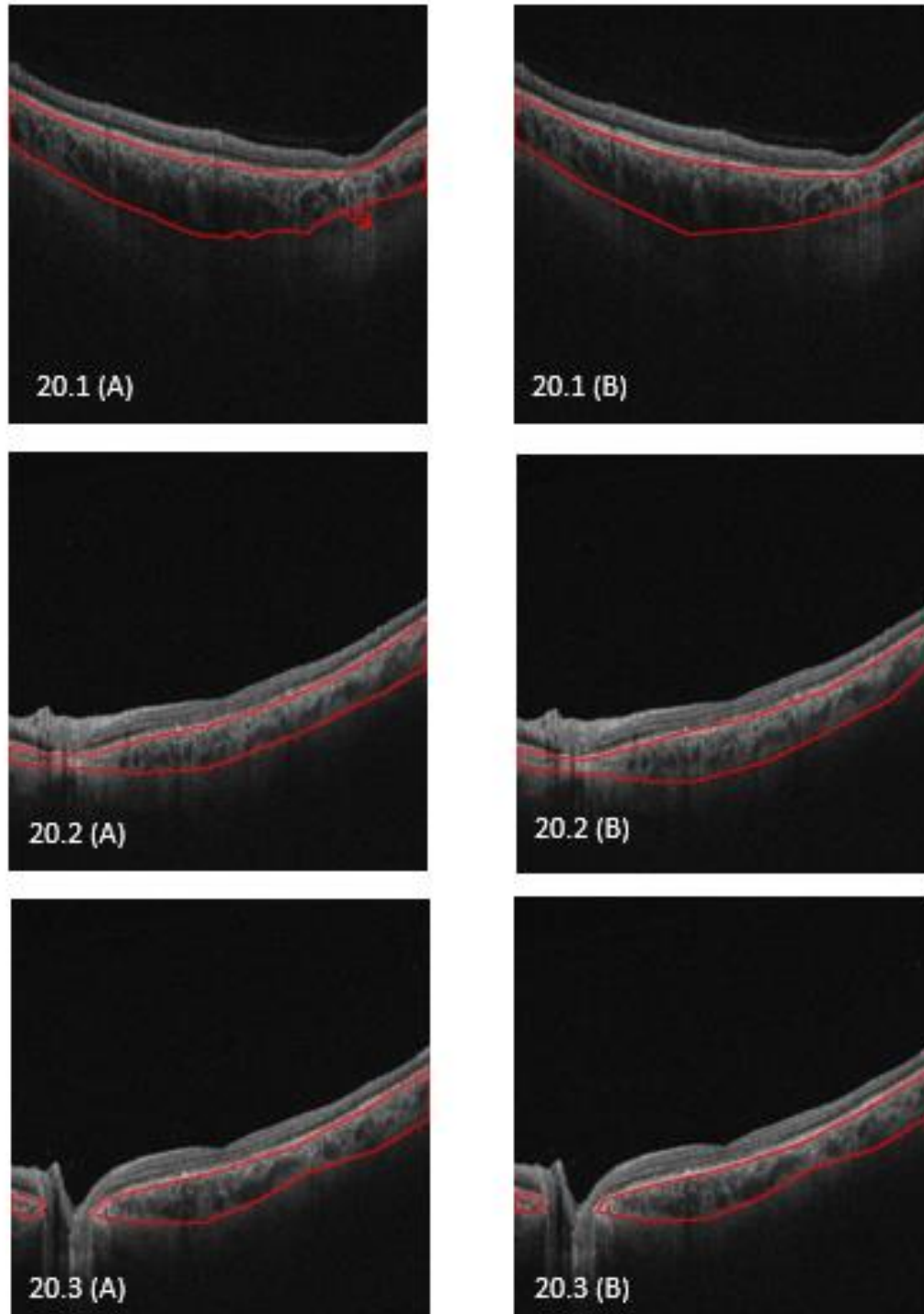


Figure 20: OCT B-scans from the validation set used annotated by the trained SegResNet (left) and annotated by field professionals (right). Figure 20.1 A and B are B-scans taken from a patient with CSCR and extreme thickening of the choroid, Figures 20.2 A and B are from an healthy subject and 20.3 A and B were taken from patient with CSCR but from the section that contains the optic nerve.

Using the best performing model and the methodology described in section 1.4.2 we generated a thickness map for every scan in the dataset. The thickness values are normalized to be a number between 0 and 1 with 1 being 120 pixels. The values were then translated into a color gradient with dark blue being 0 and red 1. The thickness maps composed of the dataset used to train the automatic choroidal hyperpermeability classification model. Figure 21 is a composition of thickness maps taken from both patients with CSCR (right) but also from healthy patients (left):

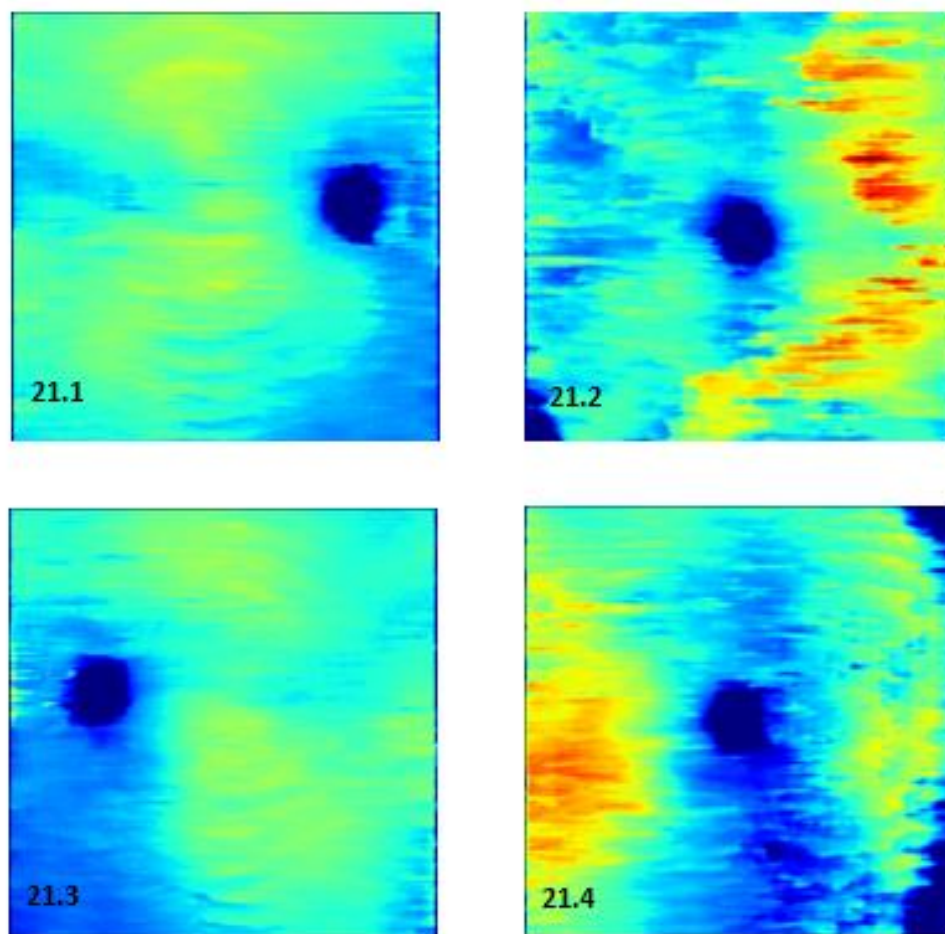


Figure 21: Thickness maps generated from patients with CSCR (right – 21.2, 21.4) and from healthy patients (left 21.1, 21.3). In most cases, patients with CSCR display a more uneven choroidal layout with areas of extreme thickness present. As shown by 21.1 and 21.3 (both taken from healthy patients) healthy choroidal thickness maps have much more distributed layout without any submit changes in thickness.

For the scans that had complementary ICGA scans we were able to align the points of choroidal hyperpermeability with the thickness maps. This exercise was done to check for relation between extreme thickening of the choroid and choroidal hyperpermeability, in line with the research conducted by Ramtohul *et al.* (2023)⁴³. In Figure 22 it is shown a composition of ICGA scans with the points of choroidal hyperpermeability annotated by professionals and the thickness maps from the same patients with those points also annotated. The images were aligned using the *enface* scan's superficial vessels which are clearly defined in both.

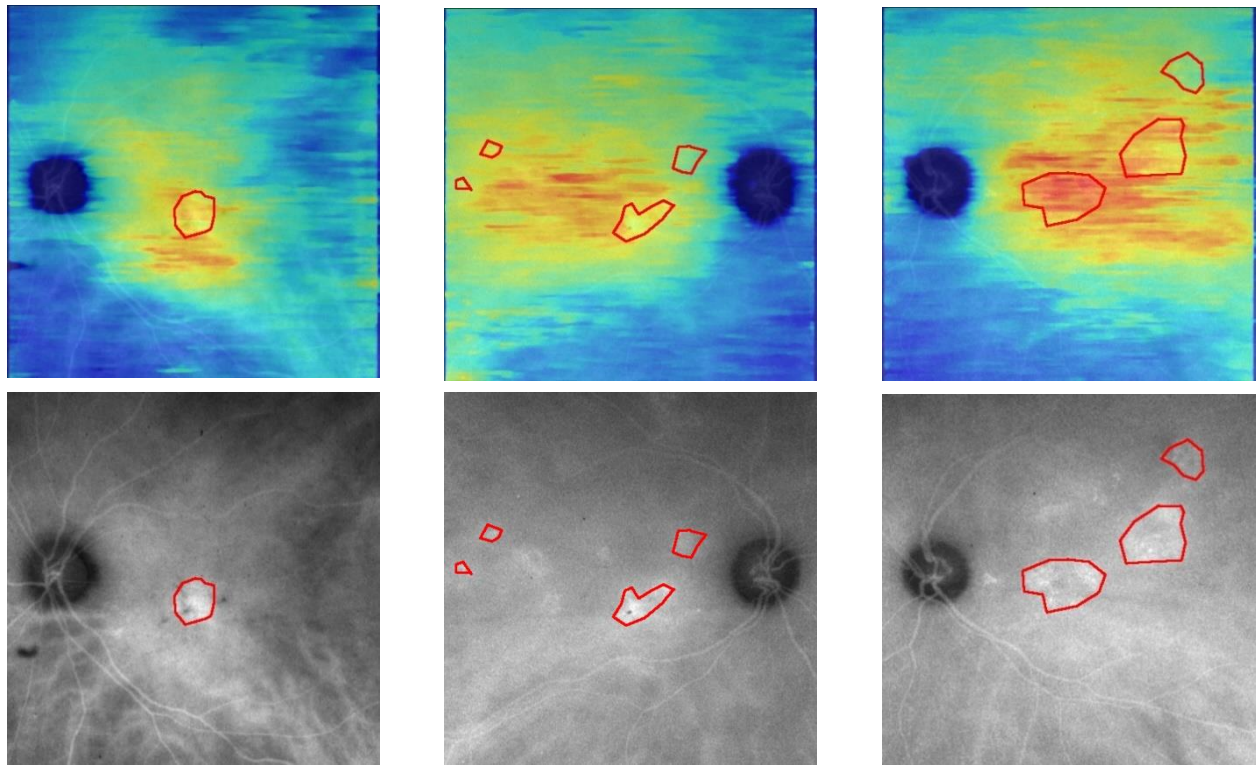


Figure 22: Thickness maps generated from patients with CSCR that have choroidal hyperpermeability points (top) and ICGA scans from the same patients with the areas annotated by professionals. The scans were aligned using the superficial vessels using the *enface* scan and ICGA. On these presented scans the areas of choroidal hyperpermeability coincide with areas of extreme thickening.

In the acquired dataset that contains the thickness maps with the choroidal hyperpermeability points annotated by professionals, these points coincided with the thicker areas in 70% of the scans which falls in line with the current literature on CSCR that states that the choroidal hyperpermeability zones are linked to areas of extreme thickening^{20,43}.

4.3 Thickness map classification Results

Table 5 contains the automatic hyperpermeability classification results obtained by the chosen classification model on the validation set (composed of 32 individual scans that we can confirm through the taking of ICGA scans the presence or not of choroidal hyperpermeability points: 16 positive and 16 negative), described in section 3.3:

Table 5: Results obtained by the trained Automatic Choroidal Hyperpermeability Detection Model. To evaluate the model the metrics used were Accuracy, Recall and Precision.

	Accuracy	Recall	Precision
Hole Dataset (30 scans)	81,25%	62,50%	100%
Positive Cases (15 scans)	62,50%	-	-
Negative Cases (15 scans)	100,00%	-	-

The model performed with high accuracy in telling if something is one thing or another. It got about 81% of them right. When it said something is positive, it was always right (100% precision). However, it missed catching all the pathology positive scans. It achieved about 63% accuracy when classifying the scans with choroidal hyperpermeability. So, it performs well at being sure when the choroid has a normal thickness pattern and distribution, however it fails to detect the pathology in a lot of the dataset.

4.4 Other Contributions

Although this project was developed using 15mm-by-15 mm scans using some simple adaptations the pipeline can be adapted to work with other scan formats. The key part when adapting to other sized scans is to observe if the segmentation model can segment the choroid given the different format. Surprisingly the model was able to segment 12mm-by-12mm and 15mm-by-9mm with surprisingly good accuracy.

This work's thickness map generator was adapted for 15mm-by-9mm scans and used to generate thickness maps for a paper titled "Widefield Swept Source Optical Coherence Tomography for Detection and Follow-up of Choroidal Granulomas" by that is currently under review for submission in the journal "Retinal Briefcases & Reports". Figure 23 is a composition of two of the thickness maps generated for that project, in those scans we can see the results of the treatments for granulomas with the left scan being before treatment and the right one after treatment.

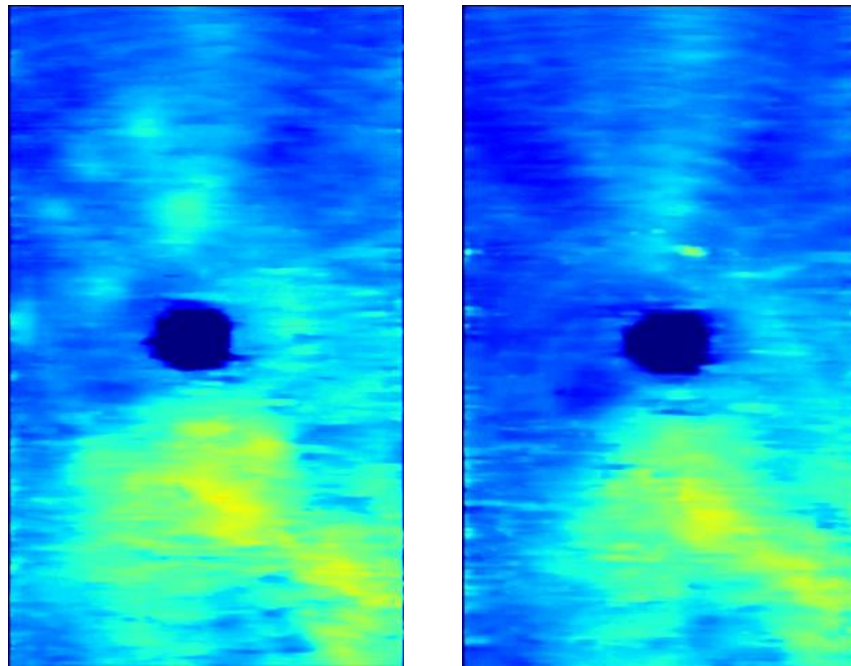


Figure 23: Composition of three thickness maps generated from 15mm-by-9mm OCT scans. This was achieved by adapting the proposed pipeline to accommodate the new sizes. Scan in the left is before the treatment and the right after treatment. The blue areas of choroidal thickening in the top half of the scan (granulomas) disappear after the therapeutics.

5. Discussion

5.1 Choroidal Segmentation Challenge results analysis

From a general overview the results were very positive and in line with the aforementioned studies in the related works section, although for a fair comparison the same datasets should be used. Masood *et al.* (2019) used a much larger, around 600 scans from 21 healthy patients, and using a patch-based approach achieved a Dice score of 97%. Healthy choroids are easier to segment due to presenting much smoother patterns and distinguishable CSJ. By comparison this work achieves a score of 94.46% with a much smaller dataset and using both healthy and non-healthy patients that had thicker and less defined choroids.

On the other hand, Kugelman *et al.* (2019) research demonstrated that deep neural semantic segmentation models outperform path-based approaches in choroidal segmentation. Which leads us to conclude that the approach of Masood *et al.* is not optimal, and thus having a 3% difference in Dice score is merely attributed to the different datasets used.

Nonetheless, comparisons with the work of Kugelman *et al.* also suffer from the previously mentioned problem, the datasets used are simply too different, both in age range and pathology. Kugelman *et al.* used scans from 101 children without any retinal or choroidal pathology and achieved a Dice score of 99%. The best performing model from the previously mentioned study was the DRUNET which was also implemented in this work and by a slight margin was outperformed by the SegResNet architecture.

Through a visual analysis of the segmented images in validation set we found that the model has a worse segmentation accuracy in the thicker areas where the CSJ is less defined, as expected. Around the optic nerve the model has shown a good capability of distinguishing where the choroid starts, and the optic nerve begins. Figure 24 contains a compilation of segmented OCT B-scans annotated by the SegResNet model, with the areas the model struggles and Figure 25 OCT B-scans where the model excels are segmenting the choroid.

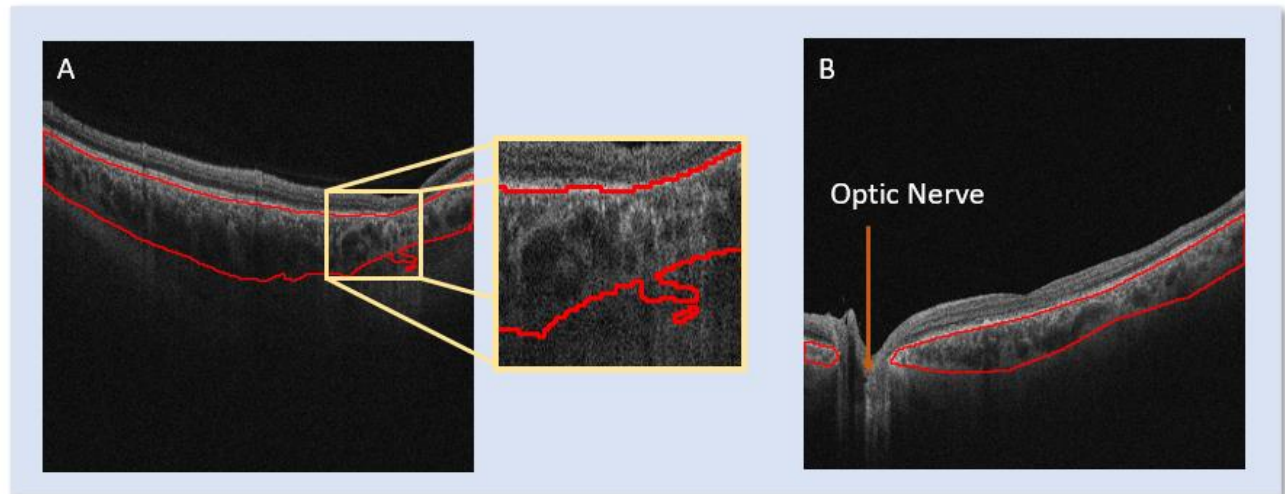


Figure 24: Composition of two automatically segmented OCT B-scans by the proposed pipeline. Figure 24-A is an OCT B-scan taken from a patient with CSCR thus having lower contrast in the CSJ in the area highlighted where the model struggles. Figure 24-B demonstrates that the model segments around the optic nerve area with high accuracy,

5.2 Thickness Map Generation and Classification result analysis

Overall, the high segmentation accuracy achieved by the best performing model, the SegResNet, guarantees that the thickness maps generated have a good degree of quality and definition. This quality can be demonstrated by the clearly defined optic nerve and also by having a coherent thickness map. A thickness map should always be smooth because the transition of thickness from adjacent B-scans should be gradual.

On some harder cases where the scan has artifacts or the CSJ is almost not perceptible the thickness map has visible banding noise and poor quality. Figure 26 is a composition of two thickness maps generated from a patient with CSCR (A being the left eye and B being the right eye). The scan had poor quality with a lot of artifacts and noise, this can happen due to the patient shaking or moving when the scan is taking place or because of deterioration of the choroid thus leading to an almost imperceptible choroid.

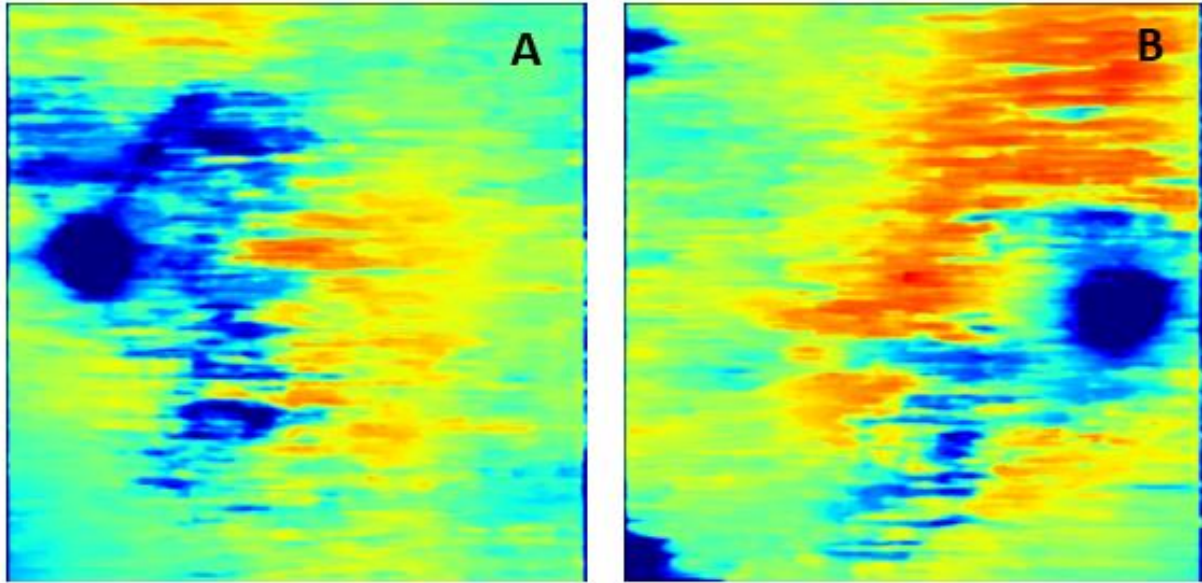


Figure 25: Two thickness maps generated from an elderly patient with CSCR. Figure 26-A is the left eye and Figure 26-B the right eye. In both cases the image is very choppy and lacks a clear and natural progression of choroidal thickness which is expected. The image has banding noise. The lack of quality can be seen by the lack of a defined optic nerve contour. This can happen when the scan has too much noise due to the patient not being able to stay still while the scan takes place.

In general, the thickness maps generated presented a good quality and due to the high segmentation accuracy provide accurate and critical information to clinicians about the choroid's morphology, thus having clinical applicability.

By generating the thickness maps from patients with choroidal hyperpermeability and juxtaposing the points with the generated maps this study found that in around 70% of the scans the points of choroidal hyperpermeability coincided with the areas of extreme thickening. These findings fall in line with current literature that state that abnormal thickening of the choroid is a biomarker of CSCR and thus having choroidal hyperpermeability points on the thicker areas is expected.

Lastly, the automatic classification results were positive, the model showed a high overall accuracy in the validation set and proved extremely capable of identifying a choroid without hyperpermeability points. Nevertheless, the high number of False Negatives demonstrates that CSCR and the presence of choroidal hyperpermeability are not always linked with an extremely abnormal pattern in choroidal thickness. In those cases, the model struggled to provide an accurate enough classification, Figure 27

illustrates two cases of CSCR with choroidal hyperpermeability but one with an abnormal thickness pattern (left) and another with an even distribution of thickness (right), very similarly to what would be considered a healthy scan. Most of the cases the model struggled to classify accurately showed an even distribution of choroidal thickness without any abnormal patterns, due to them not differing majorly with healthy pathologies, not in terms of thickness not distribution.

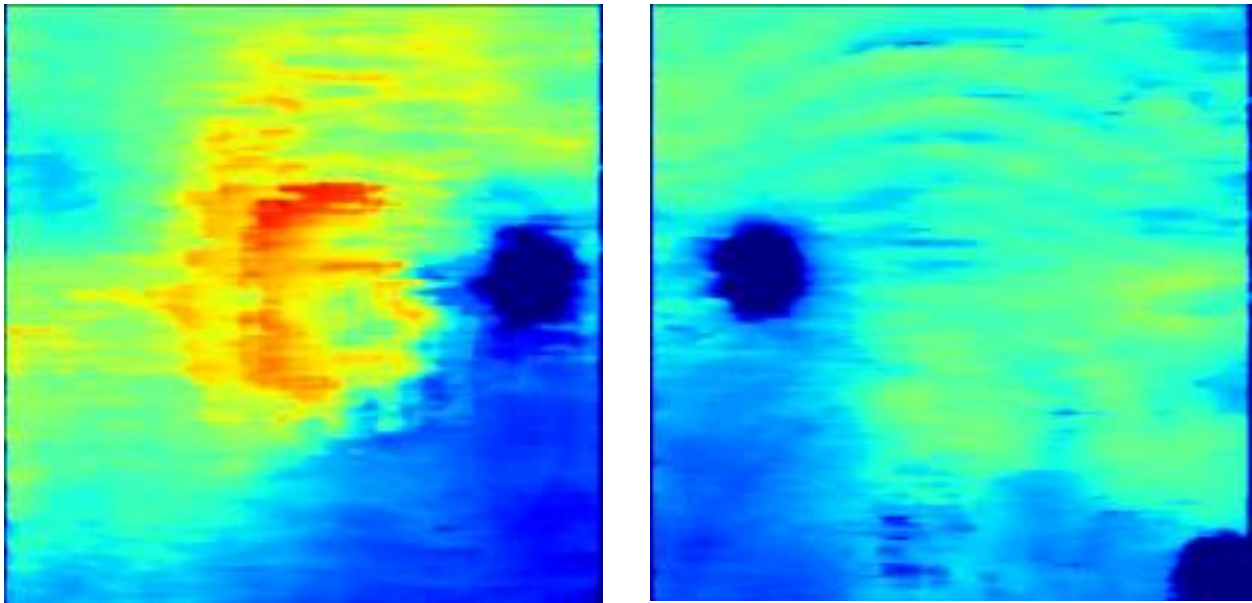


Figure 26: Two thickness maps generated by the proposed pipeline, both with points of choroidal hyperpermeability. Figure 27-A presents a central area with abnormal thickening and pattern, but Figure 27-B does not display any abnormal choroidal distribution although ICGA scan confirms the presence of choroidal hyperpermeability. These outlier cases where the thickness maps are “normal” are where the trained models struggle to identify if there are points of choroidal hyperpermeability.

Despite having good accuracy, the trained model has a lower level of recall, and struggles mostly to identify some positive cases where the thickness maps come out without any areas of abnormal thickening. This fact coupled with the maps by themselves not proving a complete picture on the pathology prevents the clinical use of such method as is. Nonetheless it helps further solidify and better understand how choroidal patterns impact the diagnosis of CSCR and strengthens the connections between points of choroidal hyperpermeability and areas of choroidal thickening.

5.3 Points of Improvement

When tackling future points of improvement to address some of the shortcomings of this work there are two ways to approach the problem. Either make improvements to the proposed pipeline or tackle the problem from a three-dimensional perspective. At the start of any problem analysis, one of the first things looked at is the available data type and what information can be extracted from it. In this case the input data are OCT raw cubic scans that in our proposed solution is converted into sectioned 2-dimensional images, called B-scans. This process is done to circumvent the hardware limitations that make working with the cubic scan impossible. By parsing the information into a 2-dimensional format we do not lose information, but we lose spatial awareness. The optimal solution would be to use a 3-dimensional convolutional approach that could take advantage of the original scans format.

Methodologies and architecture based on 3-dimensional deep convolutional neural networks have already been tried with success, for example the VoxNet has been successfully applied to 3D object recognition⁷⁹. In the field of biomedical imaging 3D convolutional networks have been successfully implemented in the early detection of Alzheimer's disease⁸⁰. The drawback of such approaches is the computational resources needed to perform such tasks.

When considering possible improvements to the proposed methodology, the first place we should look is to the datasets used. Specially on the front of the thickness maps classification, due to the lack of patients with both OCT scans and ICGA scans (do the confirm the presence of choroidal hyperpermeability points) the datasets were small to the model to have any clinical applicability. The same can be said for the pathology distribution in the datasets. Any diagnosis tool would have to be trained using thousands of cases with a multitude of choroidal and retinal pathologies. Of course, composing such a dataset would have to be the result of large-scale collaboration between a lot of investigation groups.

For the concrete example of the choroidal segmentation challenge, the largest improvement would be the inclusion of a denoising algorithm based on the light refraction levels of the top layers because most of the case where the segmentation fails the CSJ is barely perceptible. As previously mentioned, the OCT protocol is a light beam based scanning protocol, therefore one of the problems is the noise levels increase in lower layers due to photons refraction on the upper tissue layers². To tackle this issue,

previous studies applied an attenuation correction on swept source OCT scans. Zhou *et al.* (2018) two algorithms were applied to the data in order to indemnify light attenuation and to improve contrast in the images⁸¹. The method also eliminates shadows caused by light absorption from retinal vessels.

This approach significantly improved accuracy when segmenting OCT B-scans using an automated method. The results proved to be around 17% more accurate. In the following figure, Fig. 28, the difference between a normal OCT B-scan (Figure 28-A) and one treated using this method (Figure 28-B). As presented, the pixel intensity alongside the arrow is higher in the treated image. This translates into having more contrast between the sclera and the choroid. Would be an interesting proposal to do the the same project but with the algorithm proposed by Zhou *et al.* (2018) integrated in the early stages of the pipeline.

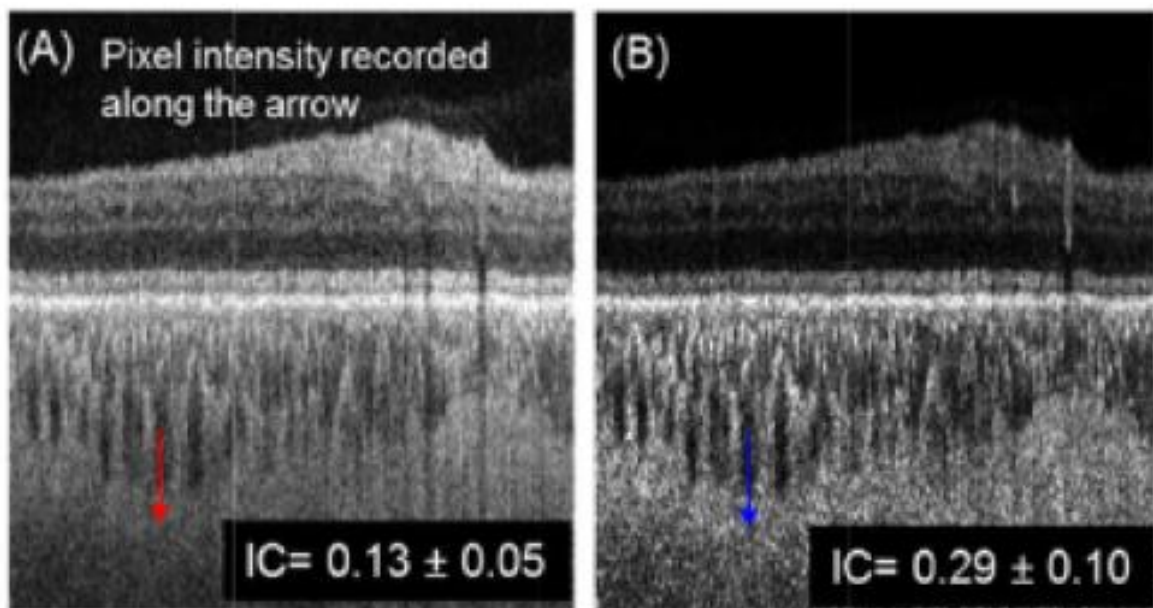


Figure 27: Two Swept Source OCT B-scans, Figure 28-A untreated and Figure 28-B with the denoising algorithm applied to it. The algorithm works especially well on increasing the average pixel contrast on the CSJ making simple segmentation techniques 17% more accurate.

6. Conclusion

The main contributions of this work are the proposal of a new methodology for automatic detection of choroidal hyperpermeability points from thickness maps as well as a study on the performance of semantic segmentation models in the task of choroidal segmentation. The proposed methodology generates two artifacts, a classification for the presence of choroidal hyperpermeability points which are a symptom of CSCR and a thickness map, through the segmentation of the choroid from OCT B-scans scans.

The results obtained by the segmentation models demonstrate that automatic segmentation has a very high accuracy even in harder cases and is very comparable to manual segmentation by professionals of the field. Furthermore, the SegResNet architecture demonstrated the best ability to tackle this challenge. Nonetheless the results can still be improved with the integration of a denoising algorithm in the preprocessing of images. In terms of the automatic detection of choroidal hyperpermeability points, the model's results clearly demonstrate the connection between extreme thickening of the choroid and abnormal choroidal patterns with choroidal hyperpermeability. However, the low recall of the model prevents it from having any clinical usability. The extremely restricted dataset, from a pathology standpoint, also limits the results achievable by the model and in the future such an approach should have in consideration a much broader plethora of retinal and choroidal pathologies.

This worked helped further our understanding of CSCR and its impact on choroidal morphology, as well as studying how choroidal hyperpermeability points are related to such abnormalities in thickness and distribution. As proposed by Ramtohul *et al.*(2023) choroidal hyperpermeability points more often than not coincide with areas of extreme thickening, with our study finding that in around 70% of the cases.

Although the proposed pipeline presents a reliable path for extracting information from OCT cubic scans, future work on the area should dive deeper into working with the volume scan without converting it into a 2-dimensional format. This would be a revolutionary approach, that given the right number of resources would most likely be able to extract the finer grained features from the scans without losing special awareness.

In conclusion, this work proposes a pipeline that proved the usefulness of machine learning in the development of complementary diagnosis tools that provide the physicians with important information, and with a limited dataset proved the capabilities of artificial intelligence in the field of optical coherence tomography imaging in replacement of invasive methods like ICGA. This study also helped further the understanding of relationships between choroidal thickness alterations and choroidal hyperpermeability points.

References

1. van Rijssen, T. J. *et al.* Central serous chorioretinopathy: Towards an evidence-based treatment guideline. *Prog. Retin. Eye Res.* **73**, 100770 (2019).
2. Aumann, S., Donner, S., Fischer, J. & Müller, F. Optical Coherence Tomography (OCT): Principle and Technical Realization. in *High Resolution Imaging in Microscopy and Ophthalmology: New Frontiers in Biomedical Optics* (ed. Bille, J. F.) 59–85 (Springer International Publishing, 2019). doi:10.1007/978-3-030-16638-0_3.
3. GER-Portugal – GRUPO DE ESTUDOS DA RETINA. <https://www.ger-portugal.com/> (2023).
4. Sociedade Portuguesa de Oftalmologia. *Sociedade Portuguesa de Oftalmologia* <https://spoftalmologia.pt/>.
5. Journal Home | TVST | ARVO Journals. <https://tvst.arvojournals.org/>.
6. Kaplan, H. J. Anatomy and function of the eye. *Chem. Immunol. Allergy* **92**, 4–10 (2007).
7. Forrester, J. V., Dick, A. D., McMenamin, P. G., Roberts, F. & Pearlman, E. Chapter 1 - Anatomy of the eye and orbit. in *The Eye (Fourth Edition)* (eds. Forrester, J. V., Dick, A. D., McMenamin, P. G., Roberts, F. & Pearlman, E.) 1-102.e2 (W.B. Saunders, 2016). doi:10.1016/B978-0-7020-5554-6.00001-0.
8. Posterior Eye Segment - an overview | ScienceDirect Topics. <https://www.sciencedirect.com/topics/immunology-and-microbiology/posterior-eye-segment>.
9. Nickla, D. L. & Wallman, J. THE MULTIFUNCTIONAL CHOROID. *Prog. Retin. Eye Res.* **29**, 144–168 (2010).
10. Damsgaard, C. & Country, M. W. The Opto-Respiratory Compromise: Balancing Oxygen Supply and Light Transmittance in the Retina. *Physiol. Bethesda Md* **37**, 101–113 (2022).
11. Kiel, J. W. *The Ocular Circulation*. (Morgan & Claypool Life Sciences, 2010).
12. BS, M. A. Z., PhD, and Philip J. Luthert, BSc, MB & Specialist, R. The Choroid in AMD: A Critical Point of Failure? <http://www.retina-specialist.com/article/the-choroid-in-amd-a-critical-point-of-failure-1>.
13. Tholozan, F. M. D. & Quinlan, R. A. Lens cells: more than meets the eye. *Int. J. Biochem. Cell Biol.* **39**, 1754–1759 (2007).
14. Zhaba, W.-D. *et al.* Retinal hypoxia after experimental subarachnoid hemorrhage. *Neurosci. Lett.* **742**, 135554 (2021).

15. Ruzafa, N., Rey-Santano, C., Mielgo, V., Pereiro, X. & Vecino, E. Effect of hypoxia on the retina and superior colliculus of neonatal pigs. *PLoS One* **12**, e0175301 (2017).
16. Kishi, S. [The vitreous and the macula]. *Nippon Ganka Gakkai Zasshi* **119**, 117–143; discussion 144 (2015).
17. Daruich, A. *et al.* Central serous chorioretinopathy: Recent findings and new physiopathology hypothesis. *Prog. Retin. Eye Res.* **48**, 82–118 (2015).
18. Kaye, R. *et al.* Central serous chorioretinopathy: An update on risk factors, pathophysiology and imaging modalities. *Prog. Retin. Eye Res.* **79**, 100865 (2020).
19. Caceres, P. S. & Rodriguez-Boulan, E. Retinal pigment epithelium polarity in health and blinding diseases. *Curr. Opin. Cell Biol.* **62**, 37–45 (2020).
20. Berger, L., Bühler, V. & Yzer, S. Central Serous Chorioretinopathy - an Overview. *Klin. Monatsbl. Augenheilkd.* **238**, 971–979 (2021).
21. Ota, T. *et al.* Subfoveal serous retinal detachment associated with extramacular branch retinal vein occlusion. *Clin. Ophthalmol. Auckl. NZ* **7**, 237–41 (2013).
22. Nicholson, B. P., Atchison, E., Idris, A. A. & Bakri, S. J. Central serous chorioretinopathy and glucocorticoids: an update on evidence for association. *Surv. Ophthalmol.* **63**, 1–8 (2018).
23. Vandewalle, J., Luybaert, A., De Bosscher, K. & Libert, C. Therapeutic Mechanisms of Glucocorticoids. *Trends Endocrinol. Metab. TEM* **29**, 42–54 (2018).
24. Busada, J. T. & Cidlowski, J. A. Mechanisms of Glucocorticoid Action During Development. *Curr. Top. Dev. Biol.* **125**, 147–170 (2017).
25. Hussain, D. & Gass, J. D. Idiopathic central serous chorioretinopathy. *Indian J. Ophthalmol.* **46**, 131–137 (1998).
26. Kapugi, M. & Cunningham, K. Corticosteroids. *Orthop. Nurs.* **38**, 336–339 (2019).
27. Canaan, S. A. Photocoagulation in retinal diseases. *J. Natl. Med. Assoc.* **54**, 71–72 (1962).
28. Lock, J. H. & Fong, K. C. S. Retinal laser photocoagulation. *Med. J. Malaysia* **65**, 88–94; quiz 95 (2010).
29. Understanding Laser Photocoagulation for Age-Related Macular Degeneration (AMD). <https://fairviewmnhs.org/patient-education/90387>.
30. Chen, G. *et al.* Subfoveal Choroidal Thickness in Central Serous Chorioretinopathy: A Meta-Analysis. *PLoS ONE* **12**, e0169152 (2017).

31. Bacci, T., Oh, D. J., Singer, M., Sadda, S. & Freund, K. B. Ultra-Widefield Indocyanine Green Angiography Reveals Patterns of Choroidal Venous Insufficiency Influencing Pachychoroid Disease. *Invest. Ophthalmol. Vis. Sci.* **63**, 17 (2022).
32. Gan, Y. *et al.* CORRELATION BETWEEN FOCAL CHOROIDAL EXCAVATION AND UNDERLYING RETINOCHOROIDAL DISEASE. *Retina Phila. Pa* **42**, 348–356 (2022).
33. Spaide, R. F., Ledesma-Gil, G. & Gemmy Cheung, C. M. INTERVORTEX VENOUS ANASTOMOSIS IN Pachychoroid-RELATED DISORDERS. *RETINA* **41**, 997 (2021).
34. Pang, C. E., Shah, V. P., Sarraf, D. & Freund, K. B. Ultra-Widefield Imaging With Autofluorescence and Indocyanine Green Angiography in Central Serous Chorioretinopathy. *Am. J. Ophthalmol.* **158**, 362-371.e2 (2014).
35. MD, M. A., MD, MBA, and Carol L. Shields. December 2017 Wills Eye Resident Case Series - Diagnosis & Discussion. <https://www.reviewofophthalmology.com/article/december-2017-wills-eye-resident-case-series-diagnosis-and-discussion>.
36. Mishra, C., Kohli, P. & Babu, N. Vortex vein ampullae seen in oculocutaneous albinism on ultrawide field imaging without angiography. *Natl. Med. J. India* **34**, 373 (2021).
37. Murtagh, P., O'Dwyer, G. & Horgan, N. Vortex Vein Ampulla. *Ophthalmology* **128**, 1707 (2021).
38. FIGURE 6. (A) Early to mid-phase UWF ICGA image of the left eye of a... *ResearchGate* https://www.researchgate.net/figure/A-Early-to-mid-phase-UWF-ICGA-image-of-the-left-eye-of-a-57-year-old-man-with-complex_fig6_357803787.
39. Lim, J. I. & Flower, R. W. Indocyanine green angiography. *Int. Ophthalmol. Clin.* **35**, 59–70 (1995).
40. Reinhart, M. B., Huntington, C. R., Blair, L. J., Heniford, B. T. & Augenstein, V. A. Indocyanine Green: Historical Context, Current Applications, and Future Considerations. *Surg. Innov.* **23**, 166–175 (2016).
41. Figure 2. Indocyanine green angiography (ICGA). The ICG-protein complex... *ResearchGate* https://www.researchgate.net/figure/Indocyanine-green-angiography-ICGA-The-ICG-protein-complex-remains-intravascular-in_fig2_351831934.
42. Baddam, D. O., Ragi, S. D., Tsang, S. H. & Ngo, W. K. Ophthalmic Fluorescein Angiography. *Methods Mol. Biol. Clifton NJ* **2560**, 153–160 (2023).
43. Ramtohul, P., Cabral, D., Oh, D., Galhoz, D. & Freund, K. B. En face Ultrawidefield OCT of the Vortex Vein System in Central Serous Chorioretinopathy. *Ophthalmol. Retina* **7**, 346–353 (2023).

44. Indocyanine Green Angiography | Department of Ophthalmology.
<https://ophthalmology.med.ubc.ca/patient-care/ophthalmic-photography/indocyanine-green-angiography/>.
45. OCT Tutorial. *Wasatch Photonics* <https://wasatchphotonics.com/oct-tutorial/>.
46. Podoleanu, A. G. Optical coherence tomography. *J. Microsc.* **247**, 209–219 (2012).
47. Deep learning in neural networks: An overview - ScienceDirect.
<https://www.sciencedirect.com/science/article/abs/pii/S0893608014002135>.
48. Apicella, A., Donnarumma, F., Isgro, F. & Prevete, R. A survey on modern trainable activation functions. *Neural Netw.* **138**, 14–32 (2021).
49. Ruder, S. An overview of gradient descent optimization algorithms. Preprint at <https://doi.org/10.48550/arXiv.1609.04747> (2017).
50. Janocha, K. & Czarnecki, W. M. On Loss Functions for Deep Neural Networks in Classification. Preprint at <https://doi.org/10.48550/arXiv.1702.05659> (2017).
51. Wang, Q., Ma, Y., Zhao, K. & Tian, Y. A Comprehensive Survey of Loss Functions in Machine Learning. *Ann. Data Sci.* **9**, 187–212 (2022).
52. Brownlee, J. What is the Difference Between a Batch and an Epoch in a Neural Network?
53. Devarakonda, A., Naumov, M. & Garland, M. AdaBatch: Adaptive Batch Sizes for Training Deep Neural Networks. Preprint at <https://doi.org/10.48550/arXiv.1712.02029> (2018).
54. A Survey of Convolutional Neural Networks: Analysis, Applications, and Prospects | IEEE Journals & Magazine | IEEE Xplore. <https://ieeexplore.ieee.org/abstract/document/9451544/>.
55. Understanding of a convolutional neural network | IEEE Conference Publication | IEEE Xplore. <https://ieeexplore.ieee.org/abstract/document/8308186>.
56. Guo, Y., Liu, Y., Georgiou, T. & Lew, M. S. A review of semantic segmentation using deep neural networks. *Int. J. Multimed. Inf. Retr.* **7**, 87–93 (2018).
57. Soulam, K. B., Kaabouch, N., Saidi, M. N. & Tamtaoui, A. Breast cancer: One-stage automated detection, segmentation, and classification of digital mammograms using UNet model based-semantic segmentation. *Biomed. Signal Process. Control* **66**, 102481 (2021).
58. Ballestar, L. M. & Vilaplana, V. MRI Brain Tumor Segmentation and Uncertainty Estimation Using 3D-UNet Architectures. in *Brainlesion: Glioma, Multiple Sclerosis, Stroke and Traumatic Brain Injuries* (eds. Crimi, A. & Bakas, S.) 376–390 (Springer International Publishing, 2021). doi:10.1007/978-3-030-72084-1_34.

59. Ronneberger, O., Fischer, P. & Brox, T. U-Net: Convolutional Networks for Biomedical Image Segmentation. in *Medical Image Computing and Computer-Assisted Intervention – MICCAI 2015* (eds. Navab, N., Hornegger, J., Wells, W. M. & Frangi, A. F.) 234–241 (Springer International Publishing, 2015). doi:10.1007/978-3-319-24574-4_28.
60. Badrinarayanan, V., Kendall, A. & Cipolla, R. SegNet: A Deep Convolutional Encoder-Decoder Architecture for Image Segmentation. *IEEE Trans. Pattern Anal. Mach. Intell.* **39**, 2481–2495 (2017).
61. Zhou, Z., Rahman Siddiquee, M. M., Tajbakhsh, N. & Liang, J. UNet++: A Nested U-Net Architecture for Medical Image Segmentation. in *Deep Learning in Medical Image Analysis and Multimodal Learning for Clinical Decision Support* (eds. Stoyanov, D. et al.) 3–11 (Springer International Publishing, 2018). doi:10.1007/978-3-030-00889-5_1.
62. Tsang, S.-H. Review: UNet++ — A Nested U-Net Architecture (Biomedical Image Segmentation). *Medium* <https://sh-tsang.medium.com/review-unet-a-nested-u-net-architecture-biomedical-image-segmentation-57be56859b20> (2019).
63. Devalla, S. K. et al. DRUNET: a dilated-residual U-Net deep learning network to segment optic nerve head tissues in optical coherence tomography images. *Biomed. Opt. Express* **9**, 3244–3265 (2018).
64. Deep Learning for Carotid Plaque Segmentation using a Dilated U-Net Architecture - Nirvedh H. Meshram, Carol C. Mitchell, Stephanie Wilbrand, Robert J. Dempsey, Tomy Varghese, 2020. <https://journals.sagepub.com/doi/abs/10.1177/0161734620951216>.
65. Wang, H., Cao, P., Wang, J. & Zaiane, O. R. UCTransNet: Rethinking the Skip Connections in U-Net from a Channel-Wise Perspective with Transformer. *Proc. AAAI Conf. Artif. Intell.* **36**, 2441–2449 (2022).
66. Myronenko, A. 3D MRI Brain Tumor Segmentation Using Autoencoder Regularization. in *Brainlesion: Glioma, Multiple Sclerosis, Stroke and Traumatic Brain Injuries* (eds. Crimi, A. et al.) 311–320 (Springer International Publishing, 2019). doi:10.1007/978-3-030-11726-9_28.
67. Caterini, A. L., Doucet, A. & Sejdinovic, D. Hamiltonian Variational Auto-Encoder. in *Advances in Neural Information Processing Systems* vol. 31 (Curran Associates, Inc., 2018).
68. Wang, L. et al. Comparative analysis of image classification methods for automatic diagnosis of ophthalmic images. *Sci. Rep.* **7**, 41545 (2017).
69. Chen, Y. et al. Automatic Design of Convolutional Neural Network for Hyperspectral Image Classification. *IEEE Trans. Geosci. Remote Sens.* **57**, 7048–7066 (2019).

70. Masood, S. *et al.* Automatic Choroid Layer Segmentation from Optical Coherence Tomography Images Using Deep Learning. *Sci. Rep.* **9**, 3058 (2019).
71. Automatic Choroid Layer Segmentation from Optical Coherence Tomography Images Using Deep Learning | Scientific Reports. <https://www.nature.com/articles/s41598-019-39795-x>.
72. Krizhevsky, A. Convolutional Deep Belief Networks on CIFAR-10.
73. Automatic choroidal segmentation in OCT images using supervised deep learning methods | Scientific Reports. <https://www.nature.com/articles/s41598-019-49816-4>.
74. Kugelman, J. *et al.* Automatic choroidal segmentation in OCT images using supervised deep learning methods. *Sci. Rep.* **9**, 13298 (2019).
75. Dr.A, .Usha Ruby. Binary cross entropy with deep learning technique for Image classification. *Int. J. Adv. Trends Comput. Sci. Eng.* **9**, 5393–5397 (2020).
76. Mehta, S., Paunwala, C. & Vaidya, B. CNN based Traffic Sign Classification using Adam Optimizer. in *2019 International Conference on Intelligent Computing and Control Systems (ICCS)* 1293–1298 (2019). doi:10.1109/ICCS45141.2019.9065537.
77. Tato, A. & Nkambou, R. IMPROVING ADAM OPTIMIZER. (2018).
78. ResNet 50 | SpringerLink. https://link.springer.com/chapter/10.1007/978-1-4842-6168-2_6.
79. Maturana, D. & Scherer, S. VoxNet: A 3D Convolutional Neural Network for real-time object recognition. in *2015 IEEE/RSJ International Conference on Intelligent Robots and Systems (IROS)* 922–928 (2015). doi:10.1109/IROS.2015.7353481.
80. Payan, A. & Montana, G. Predicting Alzheimer’s disease: a neuroimaging study with 3D convolutional neural networks. Preprint at <https://doi.org/10.48550/arXiv.1502.02506> (2015).
81. Zhou, H. *et al.* Attenuation correction assisted automatic segmentation for assessing choroidal thickness and vasculature with swept-source OCT. *Biomed. Opt. Express* **9**, 6067–6080 (2018).